Fracture Toughness and Fatigue Properties of Pipeline Base Steels and Welds in High-Pressure Hydrogen and Technologies for Improving Weld HE and IGSCC Resistance for Alternative Fuel Pipelines, #323

FINAL REPORT: Part 1

[Part 2 will be prepared separately by Oak Ridge National Laboratory (ORNL)]

December 31, 2014

Prepared for

Program Manager: James Merritt

Office of Hazardous Materials Technology

Pipeline and Hazardous

Materials Safety Administration

U.S. Department of Transportation

Contract Number: DTPH56-10-000001

Names and Addresses of Submitting Organizations:

1. Prof. Peter K. Liaw

The University of Tennessee, 406 Ferris Hall, Department of Materials Science and Engineering, The University of Tennessee, Knoxville, TN 37996-2100. Phone: (865) 974-6356, Fax: (865) 974-4115, E-mail: pliaw@utk.edu

2. Dr. Govindarajan Muralidharan

Oak Ridge National Laboratory, 1 Bethel Valley Road, Oak Ridge, TN 37831

Phone: (865) 574-4281, E-mail: muralidhargn@ornl.gov

3. Mr. Bilin Chen

The University of Tennessee, 209 Ferris Hall , Department of Materials Science and Engineering, The University of Tennessee, Knoxville, TN 37996-2100.

Phone: (865) 208-7100, E-mail: bchen9@vols.utk.edu

Disclaimer:

This document was prepared under the sponsorship of the U.S. Department of Transportation. Neither the United States Government nor any agency thereof, nor any of their employees, makes any warranty, express or implied, or assumes any legal liability or responsibility for the accuracy, completeness, or usefulness of any information, apparatus, product, or process disclosed, or represents that its use would not infringe privately owned rights. Reference herein to any specific commercial product, process, or service by trade name, trademark, manufacturer, or otherwise does not necessarily constitute or imply its endorsement, recommendation, or favoring by the United States Government or any agency thereof. The views and opinions of authors expressed herein do not necessarily state or reflect those of the United States Government or any agency thereof.

ABSTRACT

Two types of pipeline steels, Alloy B [Fe-0.05C-1.52Mn-0.12Si-0.092Nb, weight percent (wt.%)] and Alloy C [Fe-0.04C-1.61Mn-0.14Si-0.096Nb, wt.%)], were tested to understand the relationship among composition, microstructure, and fatigue resistance. Vickers hardness and nanoindentation tests were used to obtain the hardness and elastic modulus. Compact-tension (CT) specimens were employed for fatigue experiments. Different frequencies (10 Hz, 1 Hz, and 0.1 Hz) and different stress ratios [0.1 and 0.5, the stress ratio (R) is defined as the ratio between $P_{min.}$ (minimum applied load) and $P_{max.}$ (maximum applied load). $R = P_{min./}P_{max.}$] were used, and the tests were conducted in air, at room temperature. The effects of frequencies and different R ratios on crack-growth rates were compared. It is concluded that a higher R ratio leads to a greater fatigue-crack-growth rate (FCGR), while frequency does not have much influence on FCGRs. Moreover, Alloy B tends to have a better fatigue resistance than Alloy C under various test conditions. The microstructures of two alloys were investigated by optical microscopy (OM), scanning-electron microscopy (SEM), and transmission-electron microscopy (TEM). Fracture surfaces show transgranular patterns, and fatigue striations were observed under SEM.

Another type of pipeline steel, X70 [Fe-0.053C-1.52Mn-0.25Cr-0.19Si-0.089Nb, weight percent (wt.%)], was also studied. Fatigue tests were performed at different load levels, and comparisons were made between different parts of weld and base metals. Fracture surfaces were observed by SEM to identify fatigue and fracture mechanisms.

X-ray and Neutron-scattering-diffraction experiments were performed to study the deformation behavior around the crack tip of X52 [Fe-0.071C-1.06Mn-0.24Si-0.026Nb,

weight percent (wt.%)] and X70 pipeline steel. Both the hydrogen-charged sample and as-received sample were used to detect the influence of hydrogen. Results are presented in this report. High-energy X-ray diffraction experiments were performed to detect the plastic-zone information during the deformation. Results are presented in the report.

Table of Contents

A. PROJECT DETAILS

A.1 Introduction

Due to the increasing environmental and monetary costs of using the traditional fossil energy, the development of alternative energy sources is becoming more and more significant. Among them, solar and wind energies are the most promising ones to contribute to sustainable energy requirements. However, the productivity of solar and wind energies is highly dependent on natural solar and wind cycles, which are not necessarily consistent with highs and lows of energy demands. Finding ways to store energy is a critical component in solving this problem. It has been proposed that solar and wind energies can easily be used to separate water, thus generating hydrogen, which can be used as the energy-storage medium. Also, with the increased development of the hydrogen fuel-cell technology for the automobile industry, the demand for hydrogen is expected to increase. Besides, the development of the natural gas industry is also increasing rapidly. Therefore, how to transport hydrogen and natural gas to end users quickly and efficiently becomes an issue [1-5].

In the United States (U.S.), the primary way to transport natural gas and the majority of hazardous liquids is through the pipeline infrastructure. Transmission pipelines are the most economical and efficient way to transport a large amount of natural gas or hazardous liquids. With the increase in the energy consumption, the importance of pipeline systems increases. So far the system is relatively safe in U.S. Failures only occur once a year per thousand miles of pipelines [6]. However, it is noted that when failures do occur, they could result in severe environmental and safety issues. Thus, pipelines, especially those in high-consequence areas, where the pipe

failure incidents may cause death, injury, or significant property and environment damage, need to be maintained well and operated safely [7].

Protecting people and environments from the transportation of gases and other hazardous materials is the mission of The Pipeline and Hazardous Materials Safety Administration (PHMSA). It is also the starting point of our research. Currently, most pipelines are made of steels. In the case of steel pipelines, during gas transportation, the pressure fluctuation and the heating and cooling cycles of the piping system, combined with the change of other external forces, will create a fatigue process for pipeline steels. Over time, the cumulative effect of fatigue might lead to failure of the pipe. Therefore, the fatigue behavior of pipeline steels needs to be understood since once the early cracks are formed, the fatigue-crack-growth rate (FCGR) per cycle would be accelerated because of the corrosive environment [8-11].

In this project, we focused on the fatigue behavior of pipeline steels. In order to study the fatigue behavior of pipeline steels, we first need to know the factors that might influence the fatigue behavior. There are various factors that can affect the fatigue behavior [10, 12], such as metallurgical (alloy composition, microstructure, etc.), environmental, or mechanical [e.g., stress ratio (R) = $P_{min.}/P_{max.}$, where $P_{min.}$ is the minimum applied load, and $P_{max.}$ is the maximum applied load, frequency (f), residual stress, etc.] factors. In our proposed project, we focused on microstructural and mechanical factors.

A.2 Materials

There were five different steels involved in our project: X52 New, X52 Old, X70 (base and weld), X80 (Alloy B), and X80 (Alloy C). The chemical compositions of Alloy B, Alloy C, X70 base and weld metals are shown in Table 1.

For X70 materials, an X70 girth weld plate was employed in the study. The dimensions of the plate were approximately 520 mm (length), 270 mm (width), and 22 mm (thickness).

A.3 Microstructure Characterization

A.3.1 Introduction

The importance of microstructures on the properties of pipeline steels has been studied [13-16]. To study the fatigue properties of these pipeline steels. The first step is to perform the microstructure characterization.

The characterization of the microstructures of Alloys B and C was documented [17]. The samples for the as-received X70 material were machined and prepared for the microstructure analysis.

A.3.2 Experiment Methods

A.3.2.1 Optical Microscopy (OM)

Samples were sectioned and mounted. The mounted samples were polished with grit paper and 0.5 um Al_2O_3 slurry solution. The surface was etched with ~ 2 vol.% Nital (**2** ml Nitric acid in 100 ml Methanol). The phase information was revealed by optical microscopy (OM).

A.3.2.2 Transmission Electron Microscope (TEM)

The TEM samples are prepared from Alloys B and C, respectively. The fatigue results of these two samples are shown in Figure 8. The specimens were first precracked to a crack of 11mm, following which fatigue crack-growth experiments were performed at R = 0.1, f = 10 Hz until final fracture. Both of the TEM samples from Alloys B and C are prepared from specimens tested in the same loading condition.

As shown in Figure 1, the crack-growth length was around 26mm. Along the crack-growth direction, three 7.5 mm-long specimens with thickness of 3 mm were removed close to the fracture surface. The surfaces were made flat by grinding. Samples for Alloys B and C were sent to the National Central University, Taiwan, where the TEM samples were prepared, and TEM characterization was performed.

A.3.3 Results and Discussion

A.3.3.1 Microstructures of Alloys B and C

According to the results by Stalheim and his team [17], Alloy B consisted of about 90 vol.% coarse polygonal ferrites and 10 vol.% coarse acicular ferrites (a type of low carbon bainite), by volume fraction. The microstructure of Alloy C were very similar to that of Alloy B except that there is a small portion of the upper bainite (~2 vol.%), 8 vol.% coarse acicular ferrite (a type of low carbon bainite), and 90% polygonal ferrites. The upper bainites appear dark in the lighted microscope. This trend is caused by the lathe ferrite with the limited carbon precipitation between the laths since there is only 0.04 wt.% of carbon in Alloy C. The optical microscopy (OM), scanning-electron microscopy (SEM), and transmission-electron microscopy (TEM) analyses are shown in Figure 2 to Figure 5.

Some other observations were made on Alloys B and C, at The University of Tennessee. As shown in Figure 6, both Alloys show similar microstructures, mostly ferrite. It looks that Alloy B has a finer structure than Alloy C.

The TEM micrographs of samples from failed Alloys B and C similarly show the presence of upper bainite microstructure in both alloys, as can be seen in Figure 7 and Figure 8. Cell structures are observed in both Alloys B and C. The amount of the cellular structure is more in Alloy B than that in Alloy C.

A.3.3.2 Microstructures of X70 Base and Weld Metals

From Figure 9, we can see the macro picture of the cross section of the X 70 weld sample. Three regions, the base metal, heat-affected zone, weld metal, can be clearly seen. The sample of the weld is a V shape, and the width of the heat-affected zone is around 3 mm.

Figure 10 shows microstructures of different parts of the weld sample. We can see from the figure that the morphology of the grains is quite different. The base metal shows the elongation from the rolling process of the plate. The upper part of the weld was more compact-organized, while the grains in the lower part were round instead of acicular. It was argued that the lower part was tempered from the heat during the welding process of the upper part, resulting in different morphologies.

A.3.4 Conclusions

- The microstructures of Alloys B and C, X70 base and weld are investigated by OM and TEM, the following conclusions are drawn:

- The microstructures of Alloys B and C are similar. However, the grain structure of Alloy B seems to be finer than that of Alloy C. According to Literature results [17], Alloy C has a small amount of upper banites.
- Fine grain sizes are present for all the materials in our study, with the average grain size less than 10 um.
- For the X70 weld sample, the microstructures of different regions vary. The base metal shows mainly ferrites with elonged grains along the rolling direction. The upper part of the weld shows the acicular grain morphology and compact-organized structure, while the lower part of the weld exhibits rounded grains because of the tempering effect from continuous welding. Besides, it seems that carbides aggregate due to tempering, and some dark area formed.
- The TEM results for failed Alloys B and C suggest that cellular structures might be induced by deformation, and it is more easily formed in Alloy B than in Alloy C, at the same load level.

A.4 Mechanical Behavior

A.4.1 Introduction

In the process of hydrogen or natural gas transportation, the change of external loads, combined with the pressure variation, will create a fatigue process for pipeline steels, which will definitely contribute to the final failure of the steels. Thus, the fatigue property of the material needs to be improved since once the early cracks are formed, the FCGR would be accelerated because of the corrosive environments [18-20].

As the pivotal aspect of the present work, the fatigue-property evaluation is very important. Various factors would influence the fatigue behavior of pipeline steels [21-24], including microstructures, compositions, mechanics, environments, etc.. In our project, we mainly focused on the microstructure and mechanics.

Nanoindentation tests were employed to obtain the elastic modulus and mechanical behavior at the atomic scale and to compare with bulk properties. Vickers microhardness measurements and tensile tests were performed to acquire the materials' basic strength and mechanical properties. Four-point-bending tests were employed to obtain the stress versus cycles to failure (S-N) curve of X70 weld. Compact-tension (CT) specimens were used in the fatigue-crack-propagation experiments performed to study the crack-growth behavior of pipeline steels. These methods and experiments will be explained in detail in the later sessions.

A.4.2 Experiment Methods

A.4.2.1 Nanoindentation

Samples were prepared for nanoindentation tests to obtain the elastic modulus and mechanical behavior near the surface area. Data can also be used to compare to bulk properties. A Hysitron TriboScope (Minneapolis, MN) mounted on a Quesant atomic force microscope (AFM) (Agoura Hills, CA) was employed in this study. A cube-corner diamond indenter was used. Loading (10s), holding (10s), and unloading (10s) (altogether 30s) were chosen. Different loads were used to study the reaction of the material and to compare the hardness values. For each test condition, 5 to 6 indents were performed to minimize error.

A.4.2.2 Vickers Hardness

Samples were cut, mounted, and mirror polished to make sure that the surface was flat. Vickers-hardness experiments were performed on the sample at 11 different locations under a load of 500 gf [gram force], with a testing time of 15s. Data was then averaged to obtain the Vickers hardness value of the sample.

To compare the hardness of different regions of the X70 sample, we measured the Vickers Hardness along the direction normal to the fusion line, as shown in Figure 11(a). Moreover, we performed tests along the center line of the weld region to see the difference of hardness at different parts of the weld, as can be seen in Figure 12(a).

Besides, micro-hardness mapping was performed by Dr. Yanli Wang at ORNL to better understand the homogeneity of the weld region. Measurements were made for every 0.25 mm, as shown in Figure 13 (a).

A.4.2.3 Tensile Behavior

Smooth bar samples with a diameter of 3.175 mm for tension tests were cut by electron-discharge machining (EDM), as shown in Figure 14. The samples were tested at a strain rate of 1E-4/s at room temperature. The data-acquisition frequency is 2 Hz. The fracture surfaces were investigated by the scanning-electron microscopy (SEM) to identify the fracture mechanisms. Stress-strain curves were compared.

A.4.2.4 Fatigue life

In order to obtain the S-N curve of the X70 weld material. Four-point-bending specimens with a size of 4 x 4 x 30 mm were machined by EDM. Specimens were polished with 400 grit paper to make sure that the surface condition for each sample was the same. Samples were tested with a stress range from 750 MPa to 1,800 MPa.

A.4.2.5 Fatigue-crack propagation

The fatigue behavior of materials is divided into three stages: stage I (crack initiation), stage II (crack propagation), and stage III (final fracture). These three stages are of vital significance in the determination of the materials' fatigue life. When a structural component is subjected to cyclic loading, in order to assess the structural reliability, or even predict the crack-growth life, the information on fatigue-crack-growth rates is irreplaceable [25, 26].

The rates of crack propagation are very sensitive to the stress-intensity-factor range (ΔK) [27-30]. Depending on the combination of the loading condition and crack (or defect) size, the stress-intensity-factor range in a structural component can vary from the near-threshold to the high stress-intensity-factor ranges. Thus, for structural-reliability analyses, it is imperative to develop crack-propagation-rate properties in the stress-intensity ranges of interest. Moreover, fatigue-crack-growth behavior is sensitive to load or R ratio ($R = P_{min.}/P_{max.}$ where $P_{min.}$ is the minimum applied load, and $P_{max.}$ is the maximum applied load) and test environment [17, 28, 31]. It is, therefore, necessary to obtain the rates of crack propagation in the intended service conditions for reliability analyses. In the present work, the fatigue-crack-propagation behavior of pipeline steels with different microstructures will be emphasized and studied.

To obtain the FCGR results in pipeline steels, compact-tension (CT) specimens have been employed in the research. A computerized fatigue-testing system was used to develop FCGR (da/dN) properties as a function of ΔK. The detailed information of this automated experimental technique have been documented [32, 33]. The expression for

calculating ΔK in CT specimens can be found in various references [29, 30]. The stress-intensity factor (K) is obtained through the following equation [34]:

$$K = \frac{P(2+\alpha)}{B\sqrt{W}(1-\alpha)^{3/2}}(0.886 + 4.64\alpha - 13.32\alpha^2 + 14.72\alpha^3 - 5.6\alpha^4) \quad (1)$$

where P is the applied load, $\alpha = a/W$, a is the crack length, W is the specimen width, and B is the specimen thickness

$$\Delta K = K_{Max.} - K_{Min.} \quad (2)$$

where $K_{Max.}$ and $K_{Min.}$ are the maximum and minimum stress-intensity factors, respectively. Fatigue-crack-propagation experiments will be performed, according to the American Society for Testing and Materials (ASTM) Test Standard E647-99, "Standard test method for measurement of fatigue crack-growth rates" [34].

At room temperature, during fatigue-crack-propagation testing, the crack length of CT specimens was determined by an unloading-compliance method [29, 30, 34]. A clip-on extensometer was mounted on the front face of each CT specimen to measure crack-opening displacements, which, in turn, were converted into crack lengths by the compliance technique. The rate of crack-growth, da/dN, was determined by a seven-point incremental polynomial technique according to ASTM E647-99 [34]. Data acquisition and analyses were automated.

The fatigue-crack-growth experiments were conducted at 297 K, using a trianglular wave form. The sample geometry was shown in Figure 15. The CT specimen for the weld metal was machined according to Figure 16 so that the crack would grow in the weld, and two samples were machined through the thickness direction. As shown in Figure 16, the weld is a V shape. The two samples through the thickness direction were

characterized as weld (upper), as the upper sample near the outside of the pipe, and weld (lower), as the sample near the inside of the pipe.

Tests were performed on Alloy B, Alloy C, X70 base and weld pipeline steels in air. For Alloys B and C, the test frequencies in air covered 0.1, 1, and 10 Hz, and R-ratios of 0.1 and 0.5 (See Table 2). For the X70 base and weld metals, all the tests were performed with a frequency of 10 Hz, at different load levels. Test results of base metal, upper and lower parts of the weld were compared.

A.4.3 Results and Discussion

A.4.3.1 Nanoindentation

For the data analysis, we chose 4 sets of data from each load level, and calculated the average values of the elastic modulus and hardness. From the results, we found that the elastic modulus and hardness tend to drop with increasing load. Also, the value of hardness for Alloy C is greater than Alloy B for all the load levels, while the elastic moduli were around the same value.

To give a better comparison between these two alloys, we averaged the data from all the five load levels [2, 4, 5, 7, and 8 mN (millinewton)], and we found that the elastic moduli of Alloys B and C were basically the same, 183.2 GPa [gigapascal] (Alloy B) and 185.7 GPa (Alloy C), respectively. The average value of hardness for Alloy B was 4.7 GPa, while that of Alloy C was 5.8 GPa. The ratio of nano hardness (B to C) is 0.81 which is similar to that for Vickers hardness, 0.87. The properties on these two scales of hardness values seem consistent.

A.4.3.2 Vickers-Hardness

The results of Vickers Hardness tests are shown in Table 3. From the tests, the Vickers hardness of Alloy C was around 230 HV [Vickers Pyramid Number], while that of Alloy B was about 201 HV. The hardness values for X70 base, X52 New, and X52 old metals were 213.2 HV, 199.6 HV, and 179 HV, respectively. Alloy C had the highest hardness, while X52 old was the softest. The larger amounts of Mn and Cr in Alloy C might help increase the hardenability of alloy steels [35], which might explain why Alloy C is the hardest.

For the comparison of the hardness of different regions of the X70 sample, the results are shown in Figure 11. The softest part was in the HAZ, which was as low as 180 HV, while the hardest part was in the upper part of the weld region, which was as high as 285 HV. In the bulk part of the base metal, the hardness stayed around 210 HV. However, the data in the weld region exhibited significant scatter, so hardness measurements were made along the center line of the weld to investigate the hardness variation.

In Figure 12, we see that the hardness varied in different parts of the weld. It was as high as 265 HV in the upper weld, and was as low as 200 HV at the location around the center of the weld. So a micro-hardness map of the whole weld region is quite necessary in order to have a complete understanding of the mechanical behavior of the weld region.

From Figure 13 we can see the macro picture of the cross section of the X 70 weld sample and also the corresponding micro-hardness map, which was generated at ORNL. As we can see in the figure, besides those defect points where the hardness values were below 180 HV, the softest part of the weld sample located at the heat-affected Zone

(HAZ), mainly between 180 HV to 200 HV. Also, the last pass of the weld region, shown as the most upper part of the weld, was the strongest during the hardness indentation tests. The hardness values were above 280 HV, and the lower parts of the weld exhibit smaller hardness values.

A.4.3.3 Tensile behavior

The stress-strain curves of these pipeline steels were plotted in pairs. With comparison among Alloys B and C, X70 base and X70 weld, X52 new and old metals.

As can be seen in Figure 17, for the tension behavior of Alloys B and C, the ductility for both alloys is about 18.2%. While the shape of the stress-strain curve is pretty similar, Alloy C has a higher yield strength and ultimate tensile strength, 570 MPa and 650 MPa, comparing with 510 MPa and 590 MPa for Alloy B. Thus, overall, Alloy C is a stronger material than Alloy B.

Now let's compare the tensile results for X52 new and old metals. As we can see in Figure 18, the stress-strain curves for these two materials are quite different. The biggest difference is the ductility. The ductility for X52 old is more than 22%, comparing with 15% of X52 new. The yield strength and ultimate tensile strength for X52 old are 400 MPa and 520 MPa, respectively. While for the new X52, it was 560 MPa, and 590 MPa, respectively.

Tension tests were also performed for the X70 base and weld materials. From Figure 19, we see that the stress strain curves are similar, with the X70 base metal showing a higher strength and ductility. The yield and tensile strength for the X70 base metal are 536 MPa and 586 MPa. For the weld metal, they were 503 MPa and 565 MPa. The ductilities are 13% for the weld metal, and 15% for the base metal.

A.4.3.4 Four-point-bending experiments and S-N curve

Four-pointing-bending fatigue experiments were performed with different stress ranges. The results were plotted as Figure 20. The results showed that good fatigue behavior was observed for X70 weld. The fatigue-endurance limit here was 750 MPa, which is more than the yield strength of the material. With the increase of the stress range, cycles to failure were decreased.

As can be seen in Figure 20, even the stress range goes to more than 1,000 MPa, the sample can still hold for over 100,000 cycles. Ductile deformation is obvious, during the fatigue tests with the stress range more than 1,000 MPa. There is another interesting phenomenon here. The samples in this condition did not break in the center of the samples. However, it failed at approximately 1/3 and 2/3 of the length region of the sample.

Fracture surfaces were examined by the scanning-electron microscopy (SEM). Figure 21 shows the typical fracture surface. Three regions, the initiation, the crack-growth region and the fast fracture region, were clearly shown in the figure. If we enlarge the crack-growth region, as seen in Figure 22, we can see ductile fatigue characteristics. Transgranular patterns dominated the fracture mode.

A.4.3.5 Crack propagation

For Alloys B and C, The FCGR experiments were completed on two kinds of base pipeline steels [Alloy B (Fe-0.05C-1.52Mn-0.12Si-0.092Nb, weight percent (wt.%)] and Alloy C (Fe-0.04C-1.61Mn-0.14Si-0.096Nb, wt.%)] at different frequencies (10 Hz, 1 Hz, and 0.1 Hz) and different R ratios (0.1 and 0.5). The crack-growth rates (da/dN) as

a function of ΔK are shown from Figure 23 to Figure 30. During the constant amplitude crack-growth experiment, the crack-propagation rates increase with increasing ΔK.

Figure 23(a) and (b) plot the FCGR results of Alloy B at different frequencies, and at R ratios of 0.1 and 0.5 respectively. Figure 24(a) and (b) show the results of Alloy C. According to the figure, in air conditions, the frequencies did not influence the FCGRs significantly.

Figure 25(a)-Figure 27(a) plot the fatigue-crack-growth results of Alloy B at different R ratios of 0.1 and 0.5 and at frequencies of 10, 1, and 0.1 Hz. Figure 25(b)-Figure 27(b) showed the FCGRs results of Alloy C at different R ratios of 0.1 and 0.5 and at frequencies of 10, 1, and 0.1 Hz. In general, the FCGR at an R ratio of 0.5 is larger than at an R ratio of 0.1 for various frequencies. This trend is probably due to the fact that when R is larger, the mean stress will be greater for a certain maximum stress, as in this equation [36],

$$\sigma_m = \frac{1+R}{2}\,\sigma_{max} \tag{3}$$

where σ_m is the mean stress, and σ_{max} is the maximum stress. The amplitude of the mean stress plays an important role in affecting the fatigue behavior of materials. Higher mean stresses leads to greater FCGRs. It can also be explained by the larger maximum stress intensity caused by a higher R. Since the cyclic stress-intensity-factor-range, ΔK, is related to the stress ratio by

$$\Delta K = (1 - R)\,K_{max} \tag{4}$$

So the maximum stress intensity (K_{max}) will be higher as R increases, at a given ΔK [4]. And since the crack-growth rates were higher when R = 0.5, the final fracture happened at a lower ΔK than when R = 0.1.

By comparing the effect of stress ratio for Alloys B and C, especially at the frequency of 1 Hz (as shown in Figure 26), we also found that the FCGR for Alloy B did not increase as much as that for Alloy C. So it seems that Alloy B is not as sensitive to R ratio as Alloy C is.

Figure 28 to Figure 30 plot the comparison of FCGR results of Alloys B and C at frequencies of 10, 1, and 0.1 Hz and R ratios of 0.1 and 0.5. The FCGRs of Alloy C is greater than those of Alloy B in various conditions. It can also be seen from the figures that the difference in FCGRs between these two alloys is greater when the tests were performed at the stress ratio of 0.5, which also suggests that the FCGR of Alloy C increased more than Alloy B with increasing stress ratio.

From the literature survey, we know that the difference in FCGRs between Alloys B and C might be due to the variations in microstructures [32]. From the microstructural characterization of Alloys B and C, in case of the volume fraction, Alloy B was characterized by 90 vol.% coarse polygonal ferrites and 10 vol.% coarse acicular ferrites (a type of low carbon bainites), while Alloy C was characterized by a small portion of upper bainites (~ 2 vol.%), 8 vol.% coarse acicular ferrites (a type of low carbon Bainite), and 90% polygonal ferrites. So the microstructure was similar except for the small portion of upper bainites, as can be seen in Figure 4 and Figure 5. The difference in the fatigue resistance might be caused by this upper bainite influence. Another possibility might be that the amount of the cellular structure affects the fatigue resistance. Since from Figure 7 and Figure 8, we knew that the TEM results from failed samples showed that both Alloys B and C had upper bainite and cellular structures. Moreover, the amount of cellular structure is more in Alloy B than that in Alloy C. Thus,

it is also possible that the greater cellular microstructure of the Alloy B induced by the same level of load might lead to greater fatigue resistance.

Figure 31 presents the SEM images of the side-view fracture surface of Alloy C. Figure 31(a), (b), and (c) represent the micrographs of $\Delta K \sim 10$ MPa.m$^{0.5}$, 25 MPa.m$^{0.5}$, and 40 MPa.m$^{0.5}$, respectively. We can also clearly see the fracture surface becomes rougher with the increase of ΔK. Also, secondary cracks were observed at large ΔK.

Figure 32 presents the SEM image of the fracture surface of Alloys B and C, when $\Delta K = 10$ MPa.m$^{0.5}$. Both of them show transgranular patterns.

Figure 33 presents the fracture surface of Alloy B at middle ($\Delta K = 30$ MPa.m$^{0.5}$) and (b) high ΔK ($\Delta K = 45$ MPa.m$^{0.5}$). Ductile striations can be clearly seen at this higher magnification. It can also be seen that striation patterns seem more obvious at high ΔK levels.

For the case of X70 base of weld, to date, the FCGR experiments were finished on the X70 base metal under different maximum loads of 2.5, 3.5, 4.5, 5, 5.4, 6, and 7 kN, at a frequency of 10 Hz and R ratio of 0.1. The crack-growth rates (da/dN) as a function of ΔK are shown in Figure 34. From this figure, we can see that the results from different load levels were normalized by ΔK and the crack-growth rates (da/dN) as a function of ΔK curves are consistent among different load levels, which suggested that the ΔK is the critical factor that determined the FCGRs. Figure 35 plots the load level versus cycles to failure. It can be seen from this figure that the fatigue life decreases with the increasing load level. While the cycles to failure was around 10^5 cycles when $P_{max} = 7$ kN, it was more than 10^6 cycles when the P_{max} was less than 3.5 kN.

Moreover, the fatigue behavior of base metal and weld metals were compared under the same condition (P_{max} = 5 kN, R = 0.1, and f = 10 Hz). In particular, we also divided the weld group into the upper part (close to the outside of the pipe) and the lower part (close to the inside of the pipe). The comparison between the base metal and the upper part of the weld metal and the comparison between the base metal and the lower part of the weld metal are shown in Figure 36(a) and (b).

Figure 36(a) plots the fatigue-crack-growth results of the X70 base and upper weld metals. From this figure we can clearly see that the FCGR of the base metal is greater than that of the upper weld. Also, as long as it went to the stable growth region, the difference is larger at lower ΔK values, and the difference would decrease with increasing ΔK. As the ΔK reaches 50 $MPa.m^{0.5}$, the FCGRs would become almost the same.

Figure 36(b) plots the fatigue-crack-growth results of X70 base and lower weld of X70. As can be seen in this figure, the FCGR of the base metal is almost the same as that of the lower weld, for all ΔK levels. The results suggest that the upper and lower parts of the weld metal reacted differently to cyclic loading.

The reason for this trend might be related to the difference in the microstructure of base and weld metals, as can be seen in Figure 10. While the base metal was mainly ferrites, the upper weld metal was characterized by bainites, and the grain size in the weld metal is smaller, the whole structure for the upper weld metal is tightly organized. Carbides were homogeneously distributed in the sample. However, for the lower weld, the microstructure was tempered by the heat from the upper weld, the grain grows and the carbides aggregate into those dark areas.

Figure 37 and Figure 38 show the SEM images of the fracture surface of X70 base and weld metals. Figure 37 is the fracture surface at high ΔK levels, where the material was about to fail. Secondary microcracks can be clearly seen in both the (a) base-metal and (b) weld-metal images. Figure 38 shows a higher magnification of the fracture surface. Ductile striations can be seen in both figures. Also, some defects are presented in the weld metal.

A.4.4 Conclusions

- The results of nano hardness is consistent with those of Vickers Hardness.
- Of all the base steels in our study, Alloy C has the highest hardness of 230 HV, while the hardness for X52 old is the lowest, 179 HV.
- For the X70 weld sample, the hardness varies a lot. The softest part is the HAZ, which can go as low as 180 HV, while the highest hardness in the upper part of the weld can go above 280 HV.
- Good fatigue behavior was shown in this X70 weld material. For four-point-bending experiments, the fatigue endurance limit is around 750 MPa (Δσ).
- In general, frequencies don't significantly influence the FCGR behavior on the current pipeline steels (Alloys B and C).
- The two alloys exhibited different fatigue behavior in air. In general, Alloy B has slower crack-growth rates than Alloy C does, that is to say, Alloy B has a better fatigue resistance than Alloy C.
- From the fatigue-crack-growth results of Alloy B at various frequencies and different R ratios of 0.1 and 0.5, we find that FCGRs at an R ratio of 0.5 are larger than at an R ratio of 0.1.

- The scanning-electron-microscopy (SEM) images of the side-view fracture surface were taken at small, middle and large ΔK ranges, respectively. It is clear that the fracture surface becomes rougher with increasing ΔK. Moreover, secondary cracks are observed at higher ΔK.
- The fracture surfaces of both pipeline steels show transgranular patterns, and ductile striation patterns can be clearly seen at higher magnifications.
- The FCGR of the X70 base metal increases with decreasing load levels.
- Different parts of the welds act differently to cyclic loading. The upper part of the weld showed better fatigue resistance than the lower part, which is probably due to the difference of microstructures. The acicular grains and homogenously distributed carbon in upper weld are good for fatigue performance.
- The upper part of the weld showed greater crack-growth rates than the base metal at lower ΔK. As the ΔK goes over 50 MPa.m$^{0.5}$, the FCGRs would become almost the same. The FCGRs of the lower weld and base metals were very similar.
- The scanning-electron-microscopy (SEM) images show evidence of secondary microcracks at high ΔK levels.
- The fracture surfaces present transgranular patterns, and ductile striation patterns can be clearly seen at higher magnifications.

A.5 Neutron and Synchrotron Studies

A.5.1 Introduction

During the fatigue process, a plastic zone generally produces around the fatigue-crack tip, and the crack needs to pass through this plastic zone. Thus, the fatigue-crack-growth behavior is controlled by the deformation zones that exist around the crack tip.

Therefore, the size and nature of the crack-tip deformation zone have important effects on the fatigue-crack propagation.

Neutron diffraction is a unique tool to study the mechanical behavior of materials. Its deep penetration and volume averaging capabilities enable the mapping of strain distributions in situ under applied loads [37-48]. In the investigation, fatigue-crack-growth behavior of X52 [Fe-0.071C-1.06Mn-0.24Si-0.026Nb, weight percent (wt.%)] and X70 [Fe-0.053C-1.52Mn-0.25Cr-0.19Si-0.089Nb, weight percent (wt.%)] grade pipeline steels (original and hydrogen-charged) have been investigated to find the hydrogen effect on the fatigue-crack-propagation behavior of pipeline steels at VULCAN, the Engineering Materials Diffractometer at the Spallation Neutron Source (SNS), Oak Ridge National Laboratory (ORNL), as shown in Figure 39.

Besides, high-energy synchrotron has also been used due to its high resolution related to a small spatial diffraction volume [49-52]. Synchrotron X-ray has unique advantage in probing deformation at the crack tip due to its high penetration ability and focused beam size. Due to the size of the plastic zone (0.3-1 mm) around the crack tip of the current pipeline steel, a small beam size and a high spatial resolution are required to resolve the difference between the plastic zone near crack tip and other areas, for which only synchrotron X-ray can offer such capability. These experiments, together with neutron scattering experiments, greatly benefited the study of deformation behavior around the crack-tip of the pipeline CT specimen. Synchrotron X-ray experiments were performed at the Advanced Photon Source (APS), Argonne National Laboratory (ANL) which provides one of the brightest storage ring-generated x-ray beams in the world.

A.5.2 Experiment Details

A.5.2.1 Neutron Experiments

In-situ neutron-diffraction experiments were performed using the VULCAN Engineering Diffractometer at Spallation Neutron Source (SNS), Oak Ridge National Laboratory (ORNL). The experiments were divided into two parts. One were the tensile tests, which served as the reference, and the Young's modulus calculated from the test results would be further used as the basis of simulations. The other is the strain-mapping tests, which were to obtain the strain-evolution information at different locations around the crack tip during the loading-unloading process. Both experiments were conducted on as-received and hydrogen-charged samples.

Figure 40 shows a sketch of the neutron-diffraction geometry of the experiments. When the sample was loaded in the frame, it was carefully aligned so that the loading axis was oriented 45 ° to the incident neutron beam. The two stationary detector banks, which were used to record the diffraction pattern, was centered on diffractions angles of 2 $\theta = \pm 90°$. Therefore, the diffraction vectors were parallel to the through-thickness (TT, perpendicular to the loading direction) and in-plane (IP, parallel to the loading direction) directions of the sample.

A.5.2.1.1 Sample Preparation for In-situ Neutron-Diffraction Experiments

Smooth bar specimens with a diameter of 5 mm were machined from the as-received X70 and X52 pipeline steel plates. Half of them were then mailed to Andy Slifka and Elizabeth Drexler at National Institute of Standards and Technology (NIST), where they helped put in a high pressure hydrogen chamber for two weeks. Then they covered the samples with tin in order to constrict the diffusion of hydrogen. Then they

mailed samples back in a low temperature environment. The other group served as the non-charged condition.

According to the American Society for Testing and Materials (ASTM) Standards E647-99, the CT specimens with a notch length of 8 mm, a width of 38.2 mm, and a thickness of 6.3 mm were machined from the as-received X70 and X52 pipeline steel plates. Then they were all pre-cracked with ΔK = 15 MPa $m^{0.5}$, f = 10 Hz, and R = 0.1 to a crack length of 1 mm, then switched ΔK to 11 MPa $m^{0.5}$ to generate another 1 mm of crack length, resulting in a total crack length of 2 mm. The experiments were conducted, using a computer-controlled Material Test System (MTS) servohydraulic machine. Subsequently, half of the samples was mailed to the National Institute of Standards and Technology (NIST), where they were put in a high-pressure hydrogen chamber for two weeks. Then they were covered with tin in order to restrict the diffusion of hydrogen. Then they were mailed back in a low-temperature environment. The other group of the as-received samples served as the reference condition.

A.5.2.1.2 Tensile Tests

The X52 and X70 pipeline steel samples were tested, the as-received and hydrogen-charged conditions. There were four samples all together. The 5-mm horizontal and 5-mm vertical slits were used to define the incident neutron beam, and the diffracted beams were collimated by a 5-mm-radial collimator in the tensile test, creating a 125 mm^3 gauge volume. The procedure was as follows:

1. Use load control, load the sample to 8,000 N in 30 minutes.
2. Switch to strain control, deform the sample until the strain reaches 10% in an hour (for the first sample, we deformed it to 15% in an hour and a half).

3. Unload the sample to 0 N in 20 minutes.
4. The beam was at the center of the sample, and data was collected continuously.

A.5.2.1.3 Strain-Mapping Tests

Compact-tension (CT) specimens from X52 and X70 pipeline steels, as-received and hydrogen.charged, all together four samples, were employed for the in-situ neutron-diffraction strain mapping experiments at VULCAN, SNS, ORNL [53, 54]. Figure 40 shows the geometry information from the neutron-diffraction experiment. The 2-mm horizontal and 0.5-mm vertical slits were used to define the incident neutron beam, and the diffracted beams were collimated by a 2-mm-radial collimator in the strain mapping test, resulting in a 2 mm^3 gauge volume. The experiment procedure was described as follows (steps 1-3 are for hydrogen charged sample only):

1. Run the samples for 15 cycles with f = 0.2Hz.
2. Set the system as load control, then ramp 44s until the load went to 3000N, hold for 15 min.
3. Ramp 2.5 s to the load 0 N, hold for 15 min.
4. Detect the lattice-strain evolutions at 10 different locations from the crack tip for all four samples [- 1 mm, - 0.5 mm, 0 mm, 0.5 mm, 1 mm, 1.5 mm, 2 mm, 2.5 mm, 3 mm, and 3.5 mm] during one fatigue (loading-unloading) cycle (0 N, 750 N, 1,500 N, 2,250 N, 3,000 N, 2,250 N, 1,500 N, 750 N, and 0 N).
5. The beam was on the crack tip of the sample for steps 1-3. It took about two hours to collect data for one load level. Thus, a total of 18 hours were needed for one sample.

A.5.2.2 Synchrotron Experiments

For the strain mapping around the crack tip, CT specimen has been employed in the study. CT specimens were prepared to contain a crack with a length of about 5 mm at The University of Tennessee (UT). The material has an average grain size of ~10 μm. With a thickness of 2.5 mm to fit the loading grip and frame, enough signal and grains for each pattern can be obtained. Thus, when ΔP (maximum load – minimum load) = 1,080 N, the plastic-zone size is about 1 mm. The hkl lattice-strain evolutions will be measured by in-situ high-energy X-ray diffraction at the crack tip [from –0.6 mm to 1 mm, vertically and horizontally (the plastic zone and the surrounding area),] during loading-unloading. In order to clearly characterize the plastic zone, which is about 0.6 mm, a small beam size, which is 0.1 mm (horizontal) x 0.1 mm (vertical), was employed. There were three loading cycles, normal loading-unloading, overloading-unloading and normal loading-unloading. Thus, we can detect the strain evolution during loading-unloading, as well as the overload effect. The mapping was conducted at different load levels.

The bulk-average lattice strain was calculated from the reference d-spacing measured from stress free samples. Single peak fitting will be employed to analyze the results, (110), (200) and (211) peaks were fitted. MATLAB was used to plot the strain contour around the crack tip.

A.5.3 Results and Discussion

A.5.3.1 Results and Discussion for Neutron Experiments

The in-plane information was used for the analysis. Figure 41 shows the stress-strain curve of the X52 sample, with or without hydrogen-charged. It can be calculated from the two curves that the Young's moduli for these two samples are basically the

same. Meanwhile, the yield modulus for the hydrogen charged sample of X52 was slightly higher than that of original sample, as shown in Figure 41. More tests are needed to confirm that hydrogen will have an influence on the sample so that the yield strength will be increased.

The lattice parameter versus distance from the crack tip for the X52 original sample was plotted in Figure 42 and Figure 43. It can be seen from the figure that the lattice parameter increases with load and varies by locations.

By comparing the lattice parameters in these two figures, we may find that the lattice parameters were similar for both samples at locations near the crack tip, while the lattice parameters for the hydrogen-charged sample were larger at other locations. One explanation for this phenomenon is that the lattice was expanded with the absorption of hydrogen. For locations near the crack, the existence of the compressive stress may constrain the lattice expansion.

For the neutron data analysis of the X52 pipeline base steel, figures of the lattice parameter (a) versus the distance from the crack tip at different loads during loading and unloading have been plotted. Figure 44 (a) ~ (f) show the lattice parameter as a function of the distance for the X52 pipeline steel, without and with hydrogen charged, respectively. As shown in these figures, the sample was loaded from 0 N [as shown in (a)] to 3,000 N [as shown in (c)], and then unloaded back to 0 N. The lattice parameter is different for different locations. It increases with loading and decreases with unloading. Moreover, if we observe more carefully, it appears that the change of lattice parameters for X52 with hydrogen charged are different from those for X 52 without hydrogen. In order to study the difference, we set all the parameters at the first condition as the

reference and then calculate the lattice strain after one cycle, according to the equation below：

$$\varepsilon = (a_{end} - a_{beginning}) / a_{beginning} \quad (5)$$

The lattice strain as a function of distance from crack tip after one cycle is presented in Figure 45. As Figure 45 shows, after one cycle, it seemed that more tensile residual strain was induced around the crack tip after one loading-unloading cycle, which might lead to higher crack growth rates. Additional experiments are needed to confirm this trend.

A.5.3.2 Results and Discussion for Synchrotron Experiments

Figure 46 to Figure 48 showed some preliminary results of the (211) strain map around the fatigue crack tip for Alloy C before loading, during loading, and after a loading cycle. From these figures, it can be clearly seen that how the strain field changed during loading-unloading. Because the sample was precracked before the measurement, when we did the first measurement, as Figure 46 shows us, there were residual strains from fatigue cycles before the experiment. Also, Figure 47 shows that the whole region was under tension when 3,000 N was applied. Figure 48 meant that right after one loading cycle, there were a large amount of residual compressive strain, especially around the crack tip region. These are all preliminary results. However, by this way, we can accurately observe the strain evolution during loading and unloading, which will definitely help better understand the crack-tip behavior during deformation of pipeline steels.

A.5.4 Conclusions

- In-situ neutron experiments were performed on pipeline-steel samples, with and without hydrogen charged. Smooth-bar specimens were used for the tensile test, while the compact-tension (CT) specimen was employed for the strain-mapping tests.
- From the stress-strain curve of both hydrogen-charged and original sample, it was found that the yield strength was slightly increased because of the presence of hydrogen. While similar results were also found in the literature [55], other results gave opposite results that yield strength decreased due to the hydrogen effect [56].
- Strain mapping tests show that hydrogen does have an effect on the lattice parameter. The results of X52 exhibit that the lattice parameter was expanded for the hydrogen charged sample, while for those locations near the crack tip, the increase was small. It was argued that the compressive residual stress can constrain the expansion of lattice.
- Preliminary results of high-energy synchrotron show the changes of strain map during one loading cycle, for the precracked sample. The whole region was under tension when 3,000 N was applied. Right after one loading cycle, there were a large amount of residual compressive strain.

B. DEVELOPED PRODUCTS AND TECHNOLOGY-TRANSFER ACTIVITIES

B.1 Publications

- B. Chen, G. Y. Wang, Y. Wang, G. Muralidharan and P. K. Liaw, "Effect of Microstructure on the Mechanical Behavior of Pipeline steels" 2015, in preparation.
- B. Chen, G. Y. Wang, K. An, G. Muralidharan and P. K. Liaw, "Influence of hydrogen on the lattice parameter of an X52 pipeline steel" 2015, in preparation.
- B. Chen, Y. Tong, X. Xie, K. An and P. K. Liaw, "Residual stress distribution of an X70 pipeline steel weldment and effect of heat treatment" 2015, in preparation.
- B. Chen, X. Xie, G. Y. Wang, K. An and P. K. Liaw, "Investigation of crack-tip deformation by high energy x-ray diffraction" 2015, in preparation.

B.2 Presentations

- B. Chen, G. Y. Wang, G. Muralidharan and P. K. Liaw, "Study of Fatigue Behavior of Pipeline Steels " Oak Ridge Chapter of the 2011 ASM International Educational Symposium Student Poster Competition.
- B. Chen, G. Y. Wang, K. An, Y. Wang, G. Muralidharan and P. K. Liaw "Mechanical Study on Pipeline Steels" Oak Ridge Chapter of the 2013 ASM International Educational Symposium Student Poster Competition
- B. Chen, G. Y. Wang, K. An, Y. Wang and P. K. Liaw "Studying Hydrogen Effects on the Deformation Behavior of Pipeline Steels by Neutron-Diffraction Measurements" The American Conference on Neutron Scattering (ACNS) , 2014.

- B. Chen, et al. and P. K. Liaw “Fatigue Study on Pipeline Steels” Materials Science & Technology (MS&T) Conference, 2014.
- B. Chen, G. Y. Wang, K. An, Y. Wang and P. K. Liaw “Fatigue Behavior of an X70 Pipeline Steel” TMS Annual Meeting & Exhibition, 2015.

C. GRAPHICAL MATERIALS LISTS

Table 1. The chemical compositions of four kinds of pipeline steels studied [weight percentage (wt.%)]

Element	Alloy B	Alloy C	X70 Base	X70 weld
C	0.05	0.04	0.053	0.141
Mn	1.52	1.61	1.52	0.79
Cr	0.25	0.42	0.25	0.13
S	0.003	0.002	0.005	0.009
Si	0.12	0.14	0.19	0.08
Cu	0.23	0.22	0.24	0.06
Ni	0.14	0.12	0.15	0.72
V	0.001	0.000	0.001	0.002
Nb	0.092	0.096	0.089	0.002
Al	0.036	0.037	0.054	0.001
P	0.007	0.010	0.005	0.009
Mo	0	0.01	0.008	0.108
Ti	0.012	0.015	0.018	0.006
B	0.0001	0	0.0001	0.0001
Sn	0.003	0.004	0.006	0.003
Ca	0.0016	0.0032	0.0011	0.0001
N2	0.0038	0.0030	0.008	0.018
Co	N / A	N / A	0.003	0.005
W	N / A	N / A	< 0.01	< 0.01
Sb	N / A	N / A	0.002	0.001
As	N / A	N / A	0.003	0.007
Zr	N / A	N / A	0.001	0.001
Pb	N / A	N / A	0.001	0.001
O	N / A	N / A	0.002	0.15

Table 2. Summary of fatigue tests performed in air atmosphere

Test Type	**Environment**	**R-ratios**	**Frequencies (Hz)**	**Pressure (types)**	**Steels (types)**	**Minimum Tests***
Fatigue tests	Air	0.1	0.1	n/a	2	2
	Air	0.1	1	n/a	2	2
	Air	0.1	10	n/a	2	2
	Air	0.5	0.1	n/a	2	2
	Air	0.5	1	n/a	2	2
	Air	0.5	10	n/a	2	2

Table 3. Vickers Hardness (HV) Results for Pipeline Steels

Material	**Alloy B**	**Alloy C**	**X70 Base**	**X52 New**	**X52 Old**
Vickers Hardness (HV)	201.2	229.9	213.2	199.6	178.8
Error	2.6	3.8	2.03	3.92	5.53

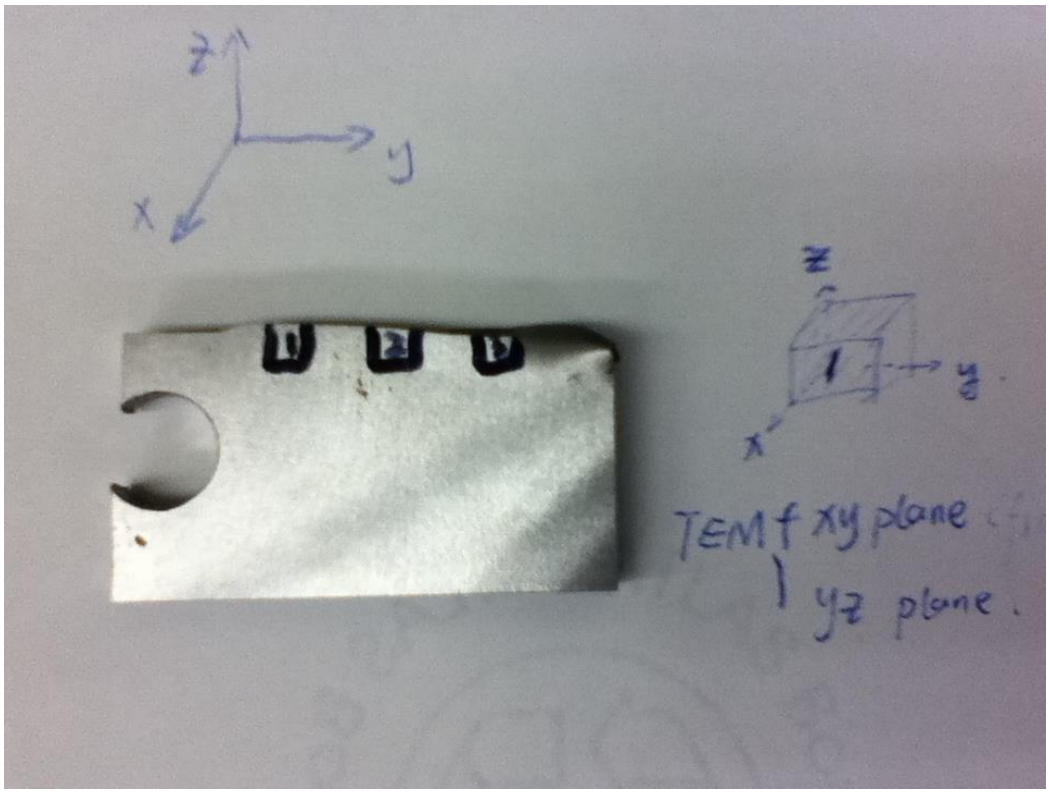

Figure 1. Locations for TEM sample preparation (Alloys B and C)

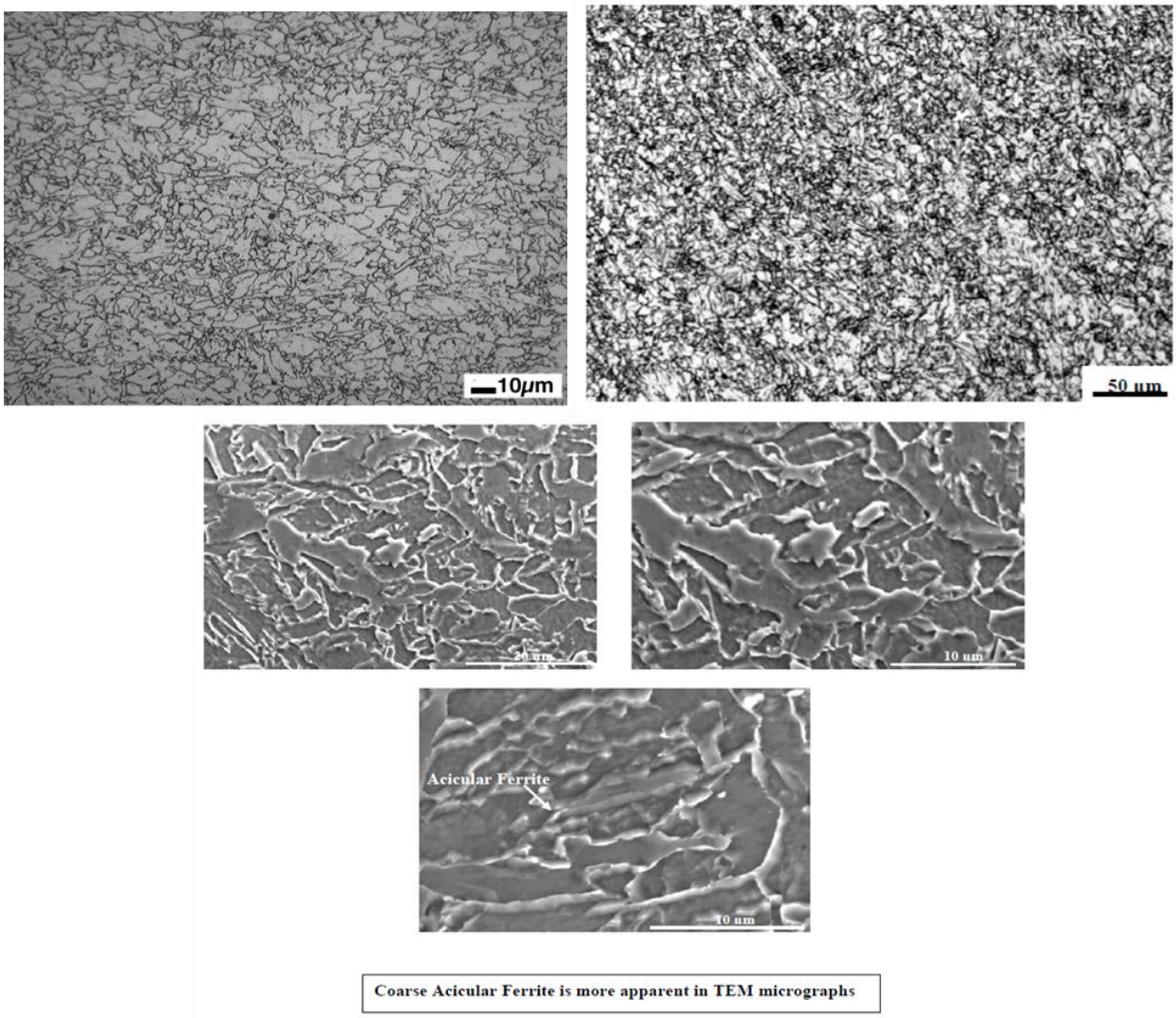

Figure 2. Optical microscopy (OM) image (upper two) and SEM image (lower three) of Alloy B. (mainly polygonal ferrite and acicular ferrite) Literature results from [17]

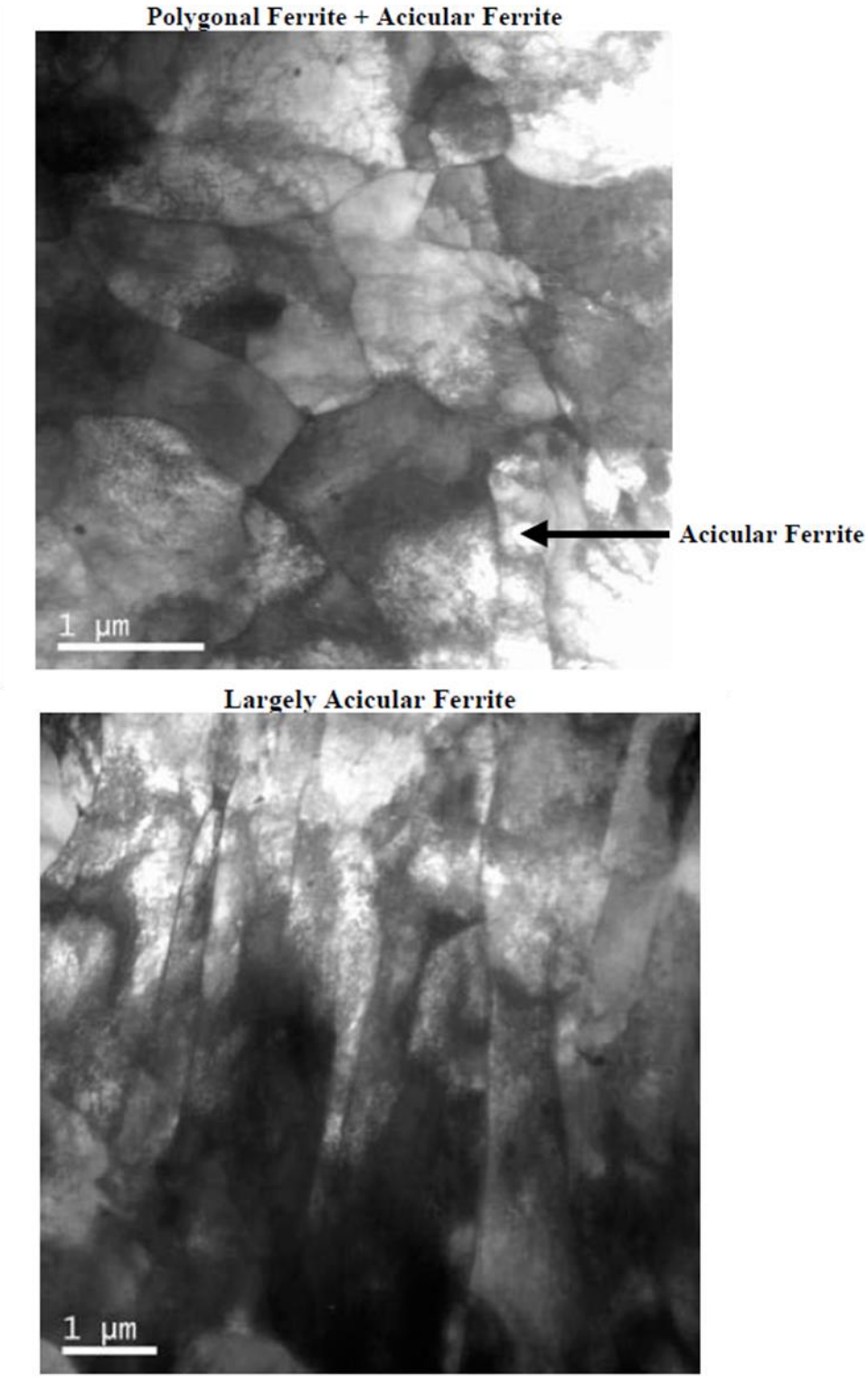

Figure 3. TEM image of Alloy B. Literature results from [17]

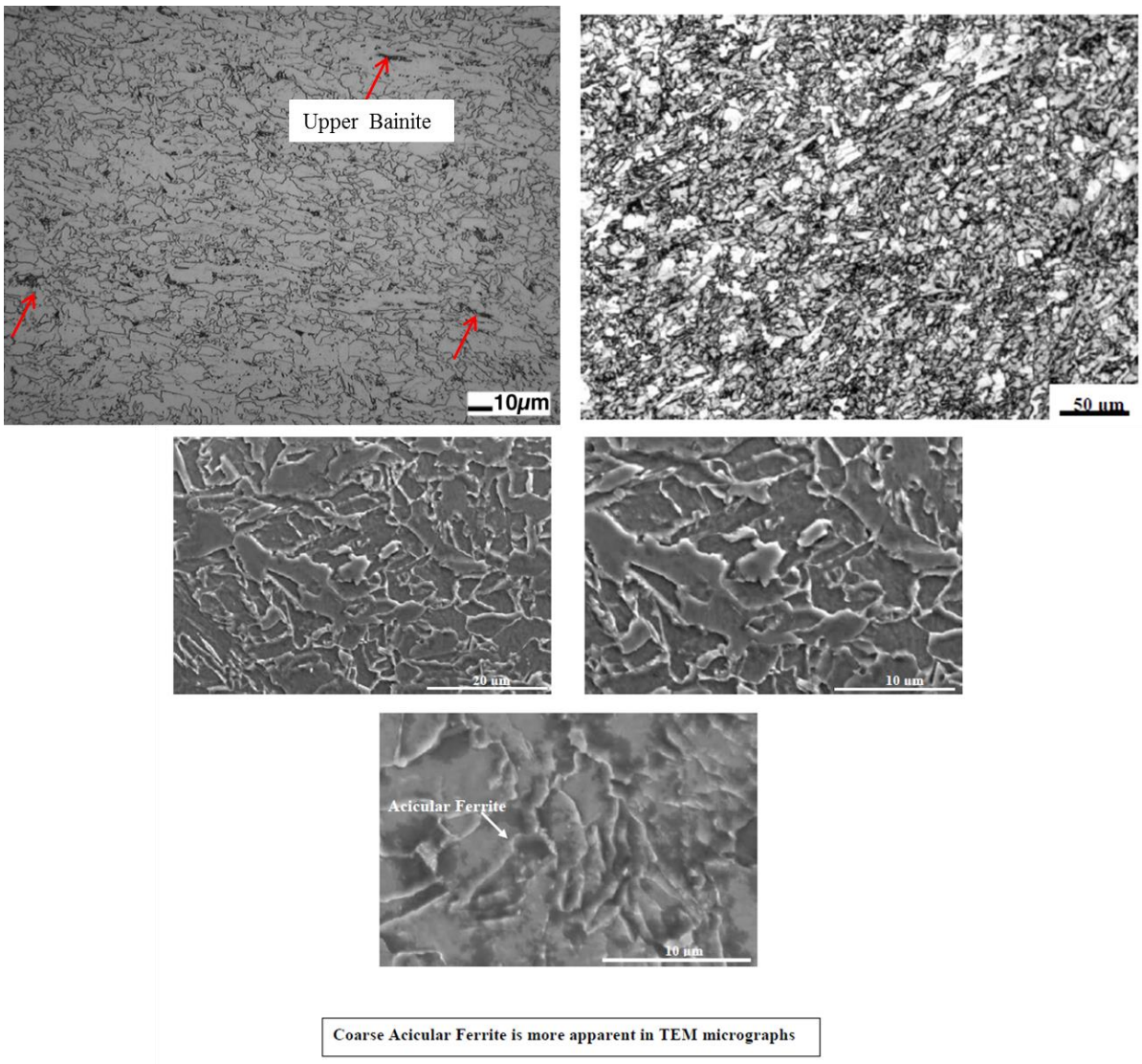

Figure 4. OM (upper two) and SEM (lower three) images of Alloy C. (polygonal ferrite + acicular ferrite + small amount of upper bainite) Literature results from [17]

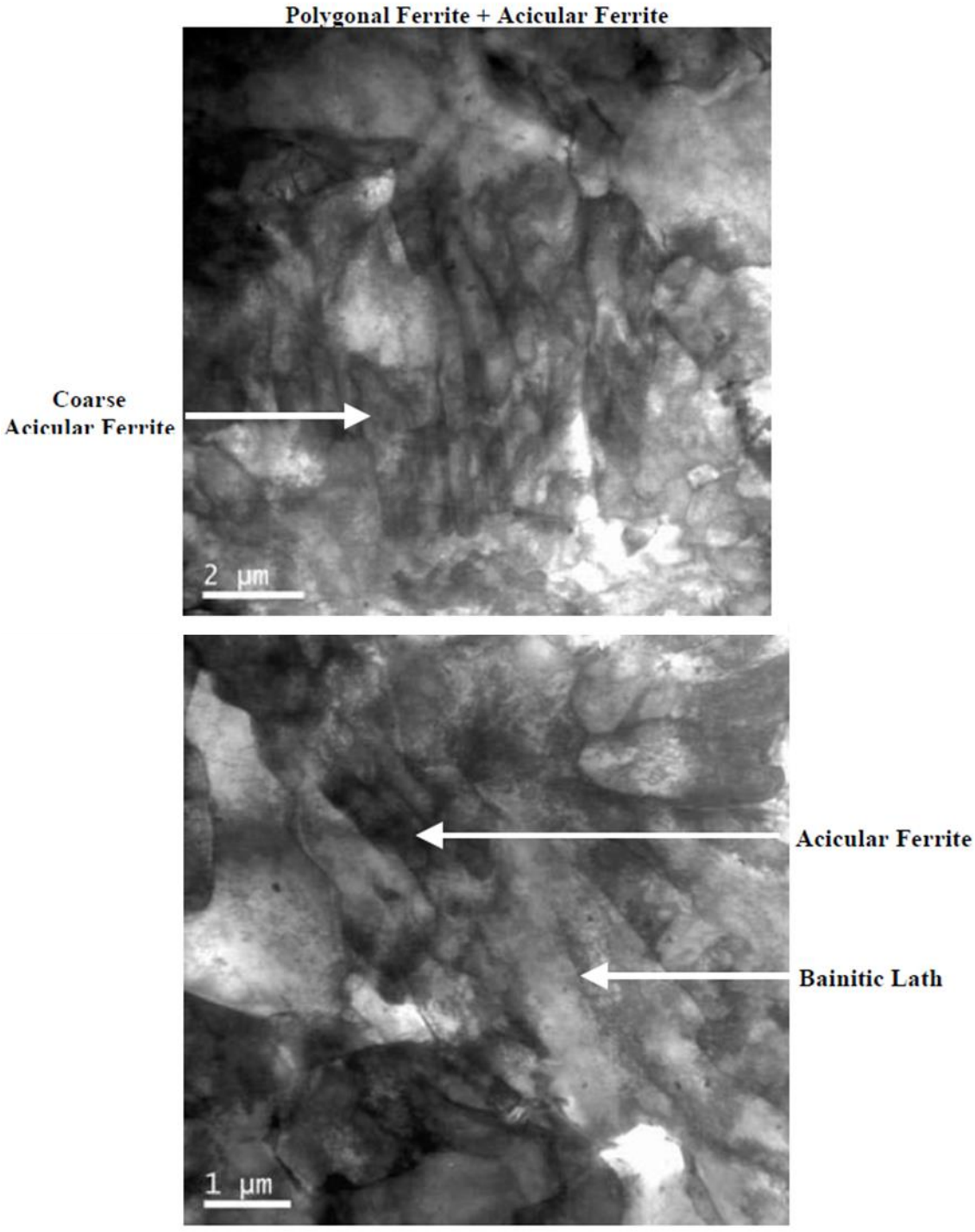

Figure 5. TEM image of Alloy C. Literature results from [17]

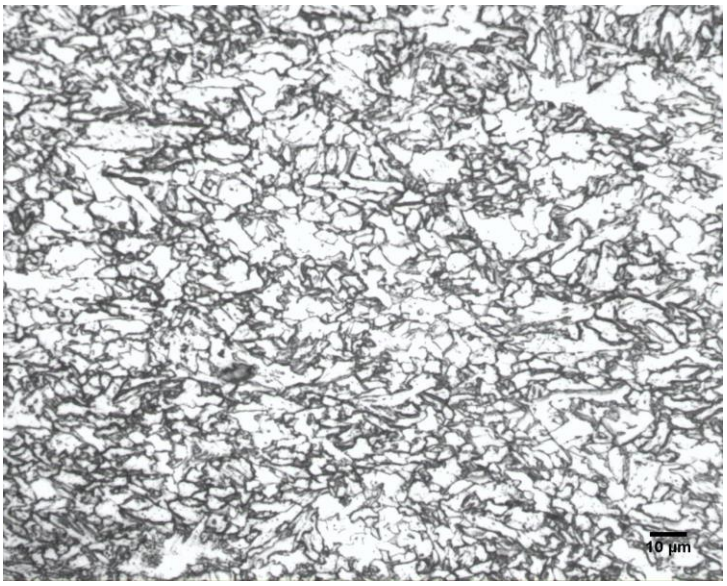

(a) Alloy B

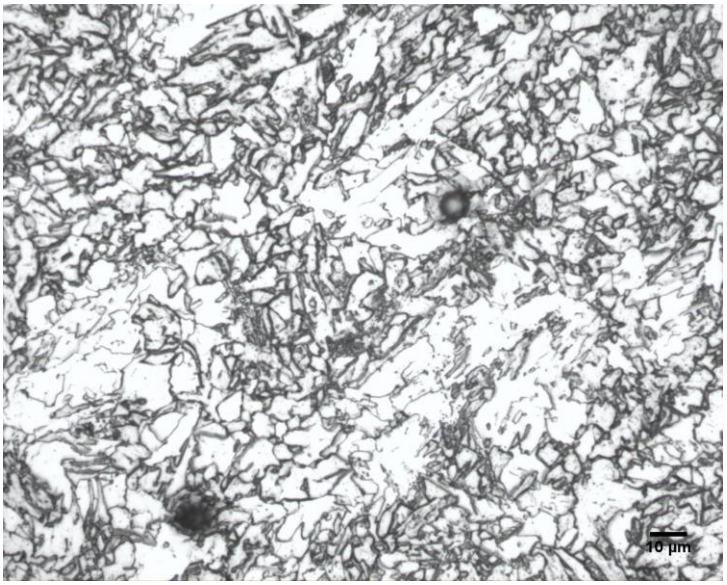

(b) Alloy C

Figure 6. OM image of Alloys B and C

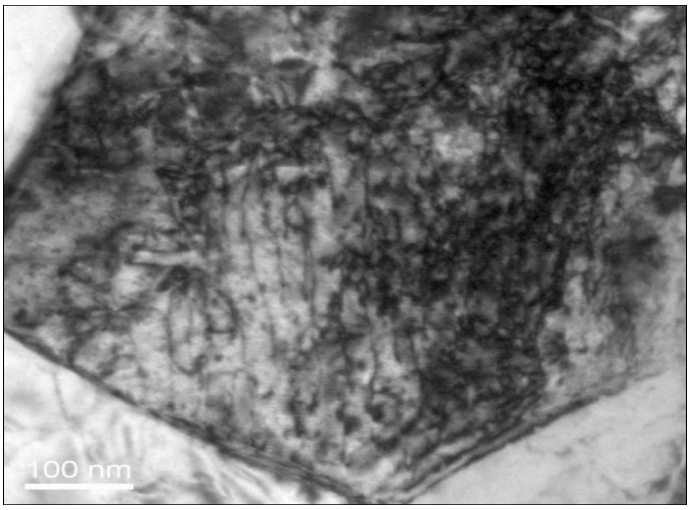

(a)

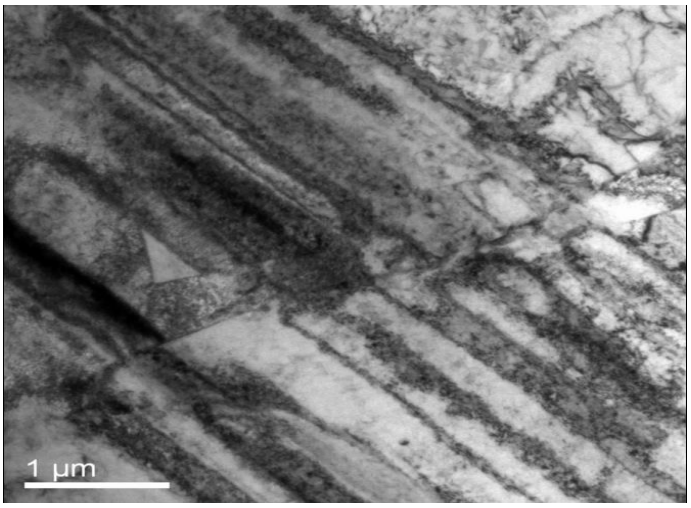

(b)

Figure 7. (a) The Upper Bainite and Bainite Lath (b) The cellular microstructure seen in Alloy B.

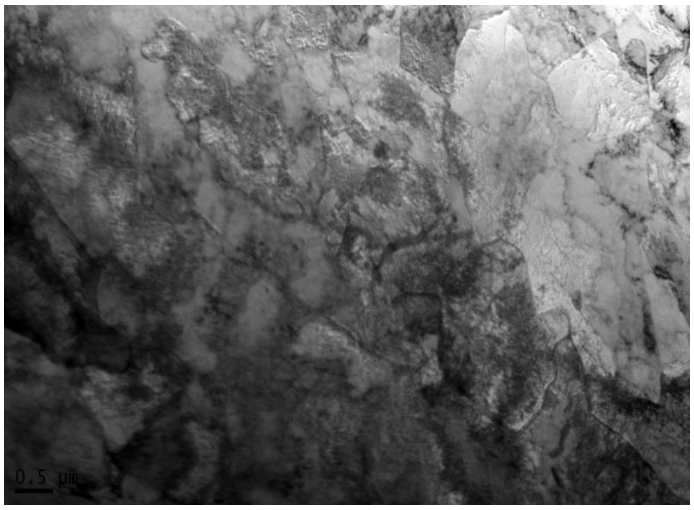

(a)

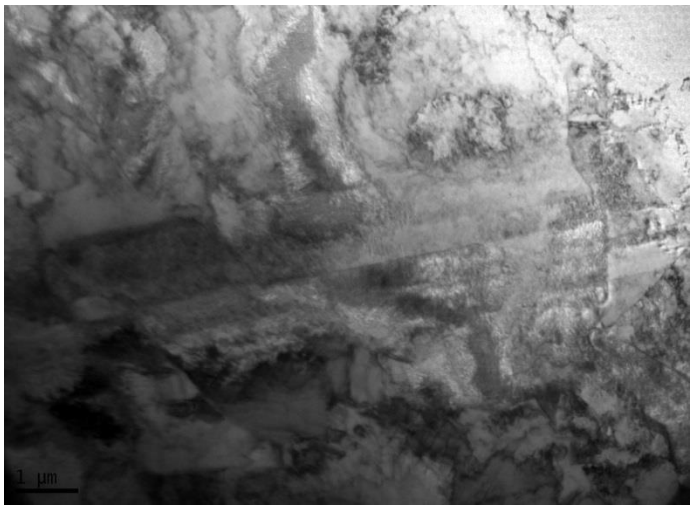

(b)

Figure 8. The Upper Bainite and Bainite Lath (b) The cellular microstructure seen in Alloy C.

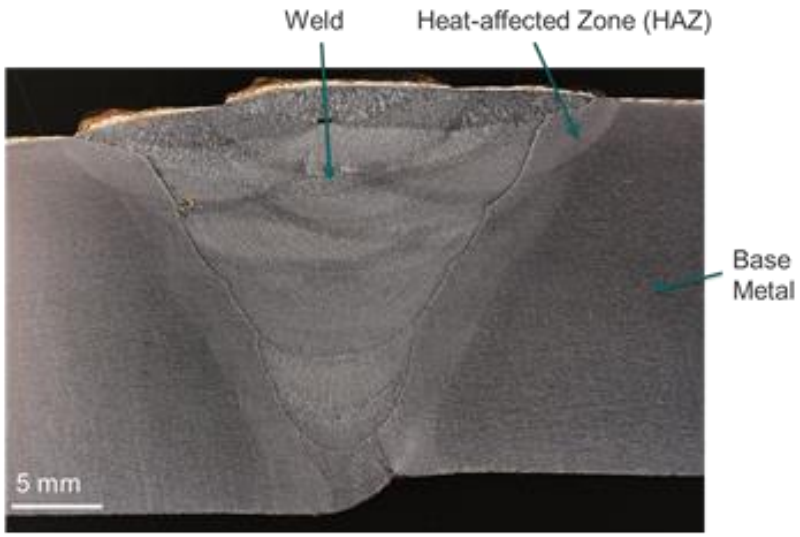

Figure 9. Macro graph of X70 weld sample

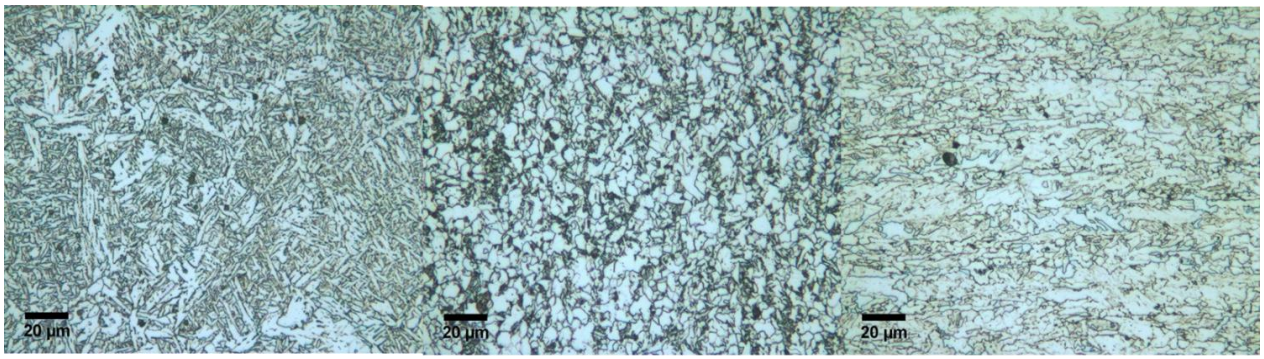

Figure 10. Microstructure of different parts of the X70 weld sample

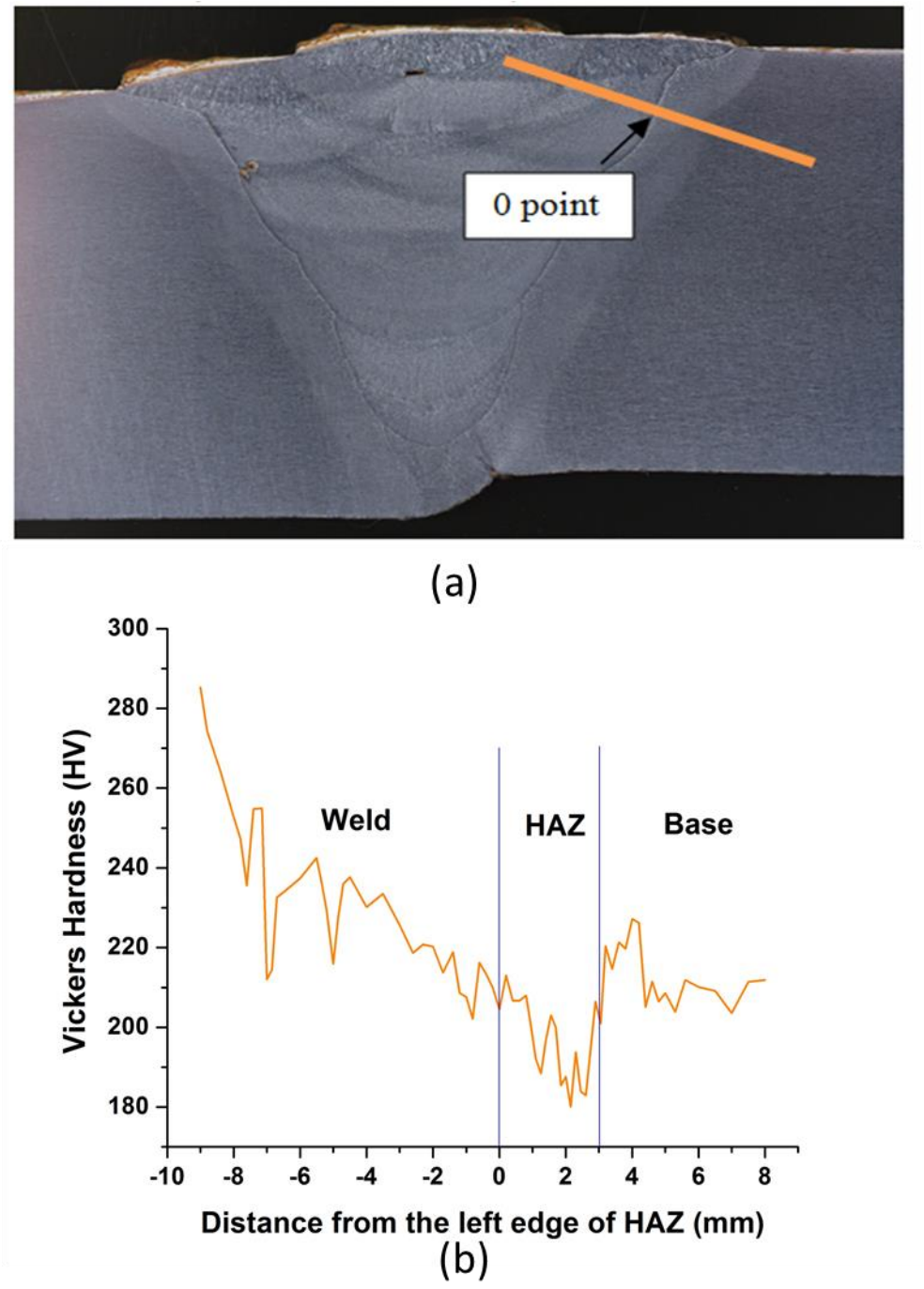

Figure 11. (a) Macro-picture of the sample; (b) Vickers hardness as a function of the distance from the left edge of heat-affected zone (HAZ) [the 0 point in (a)]

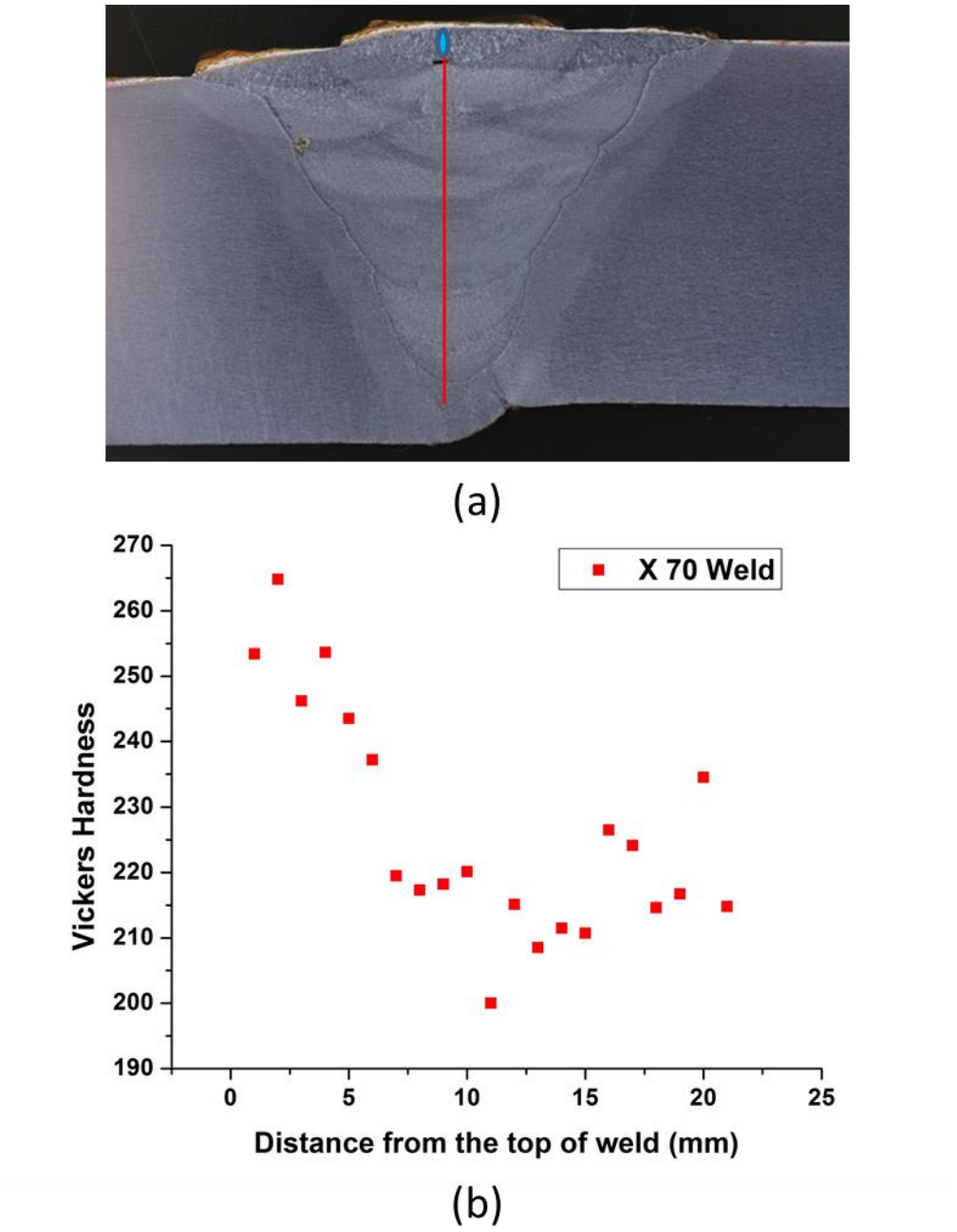

Figure 12. (a) Macro-picture of the sample; (b) Vickers hardness versus the distance from the top of the weld [the blue point in (a)]

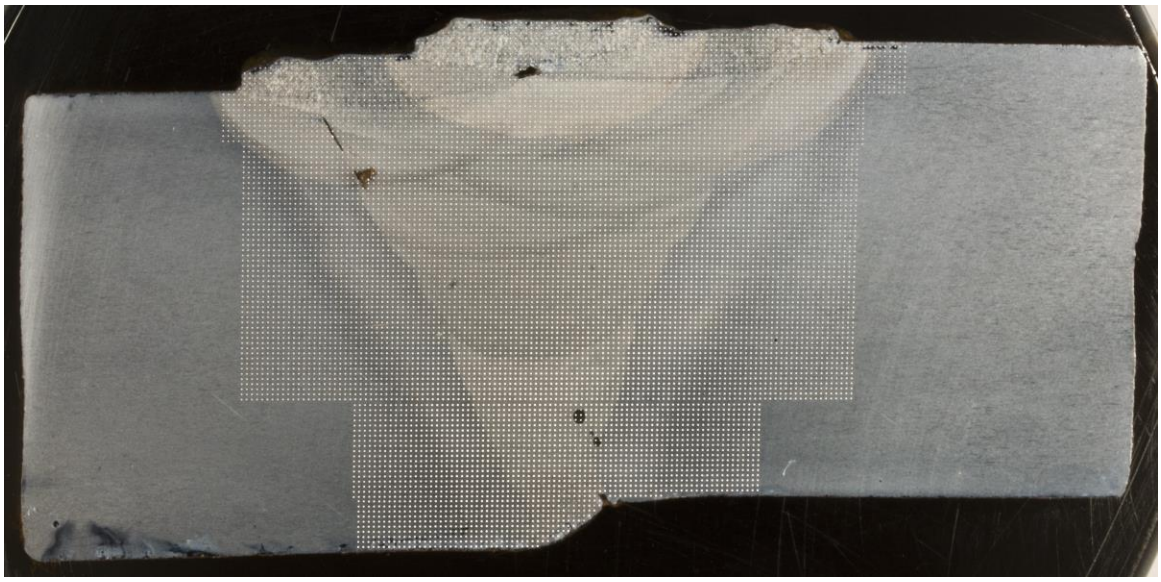

(a)

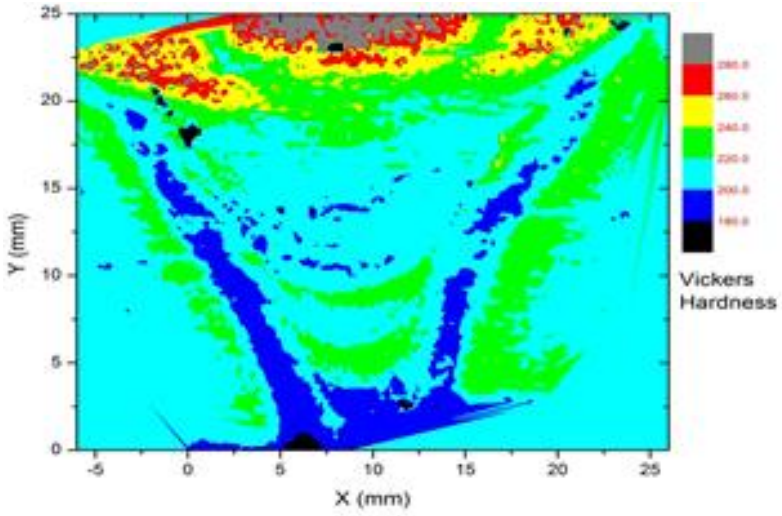

(b)

Figure 13 (a) Measurement locations of micro hardness for X70 weld sample, (b) The micro hardness map (Measured by Dr. Yanli Wang at ORNL)

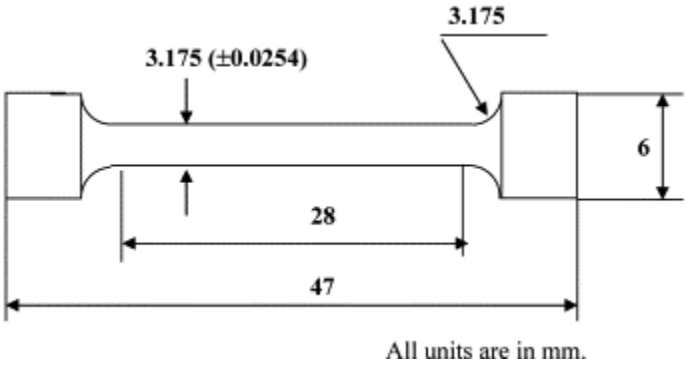

Figure 14. Specimen geometry for the smooth bar

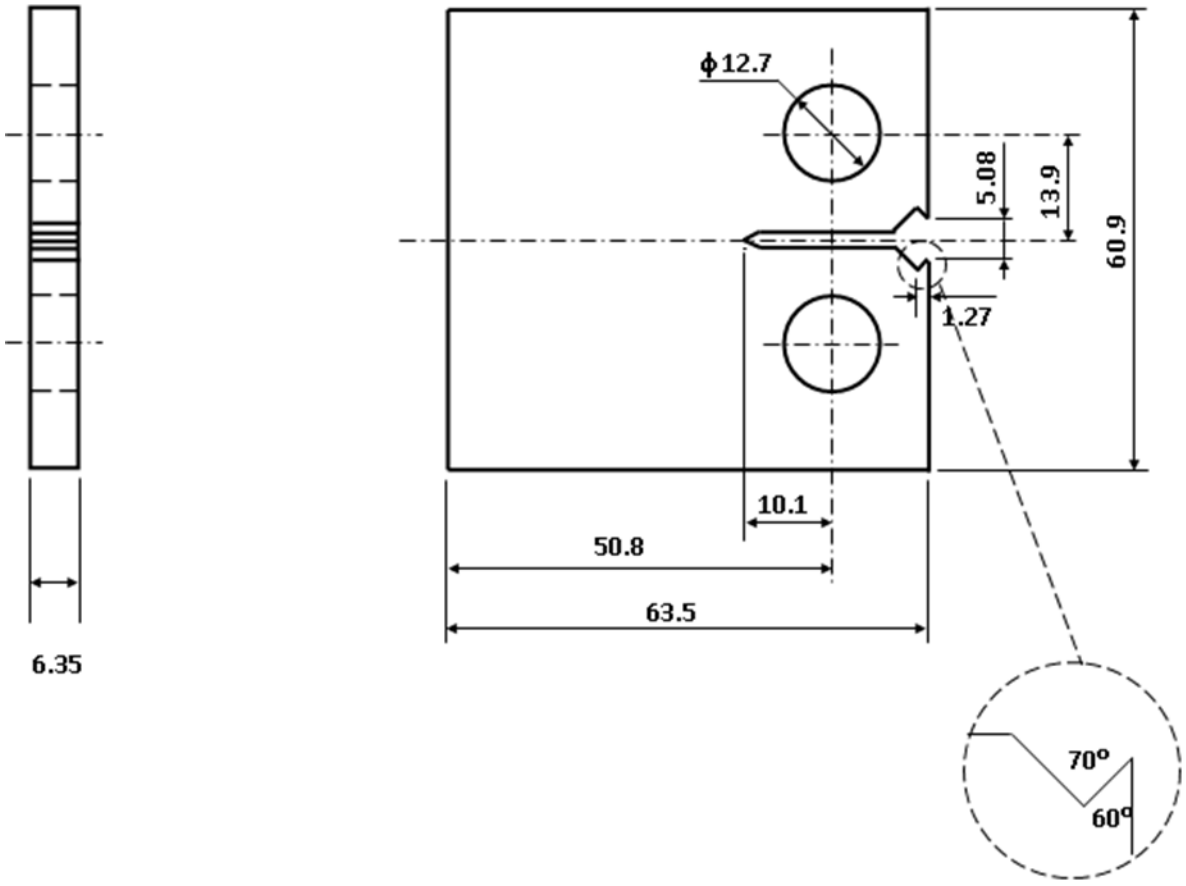

Figure 15. Geometry of the compact-tension (CT) specimen for fatigue experiments (unit: mm)

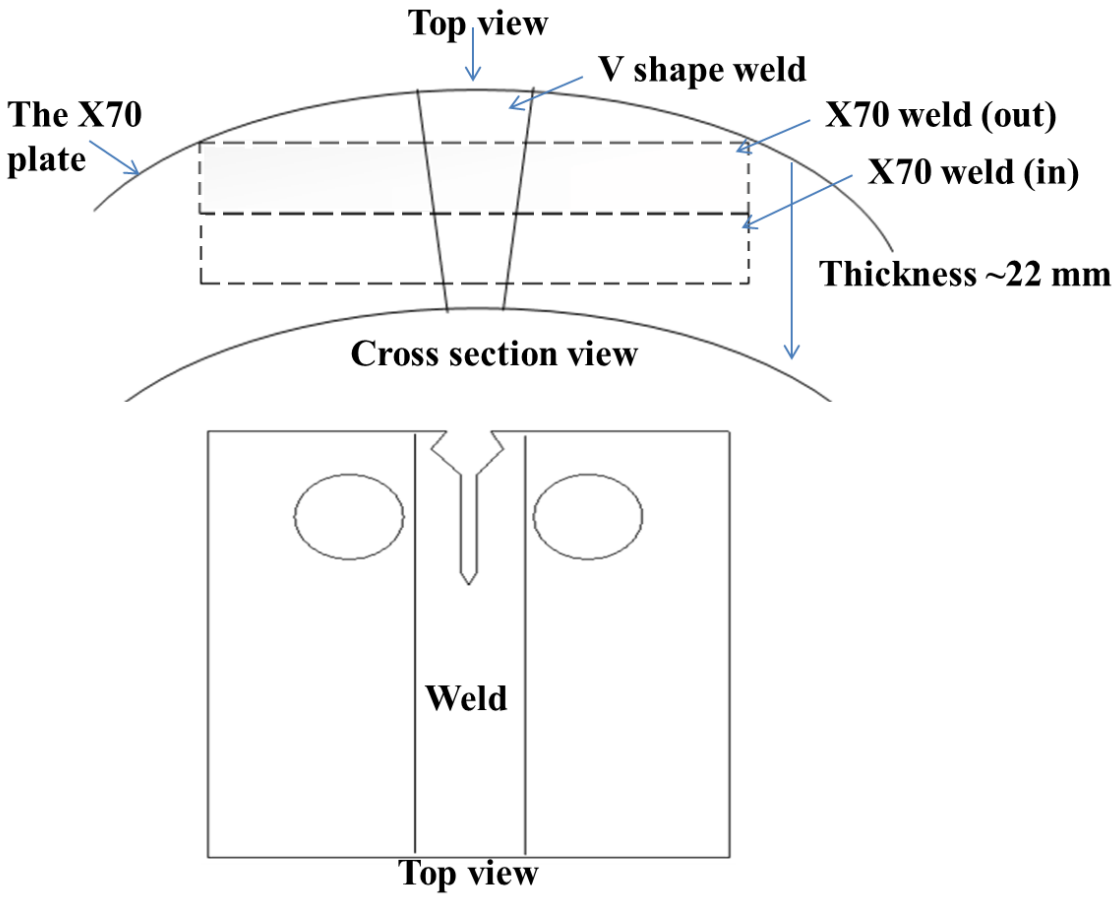

Figure 16. Sketch for the machining of the X70 pipeline steel weld sample

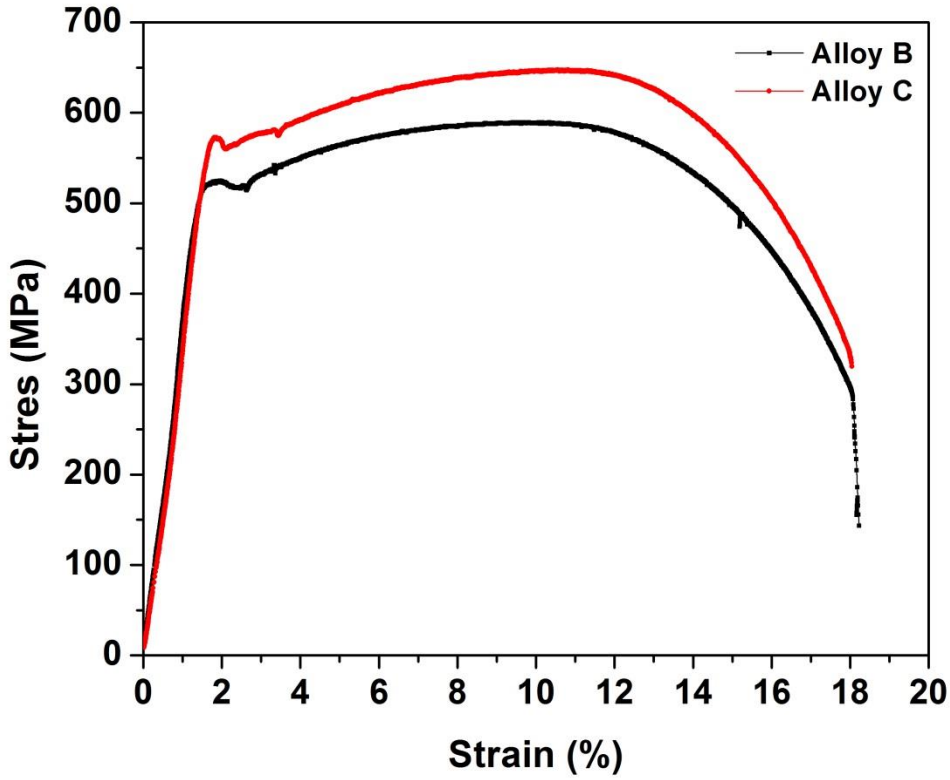

Figure 17. Stress strain curves for Alloys B and C

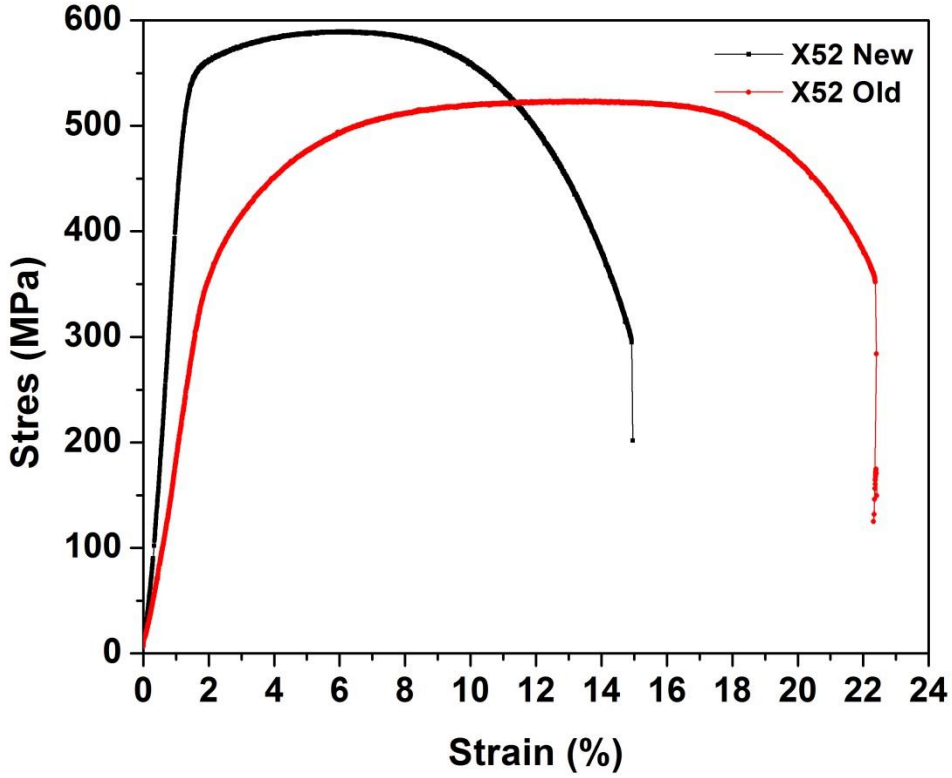

Figure 18. Stress stain curves for X52 old and new metals

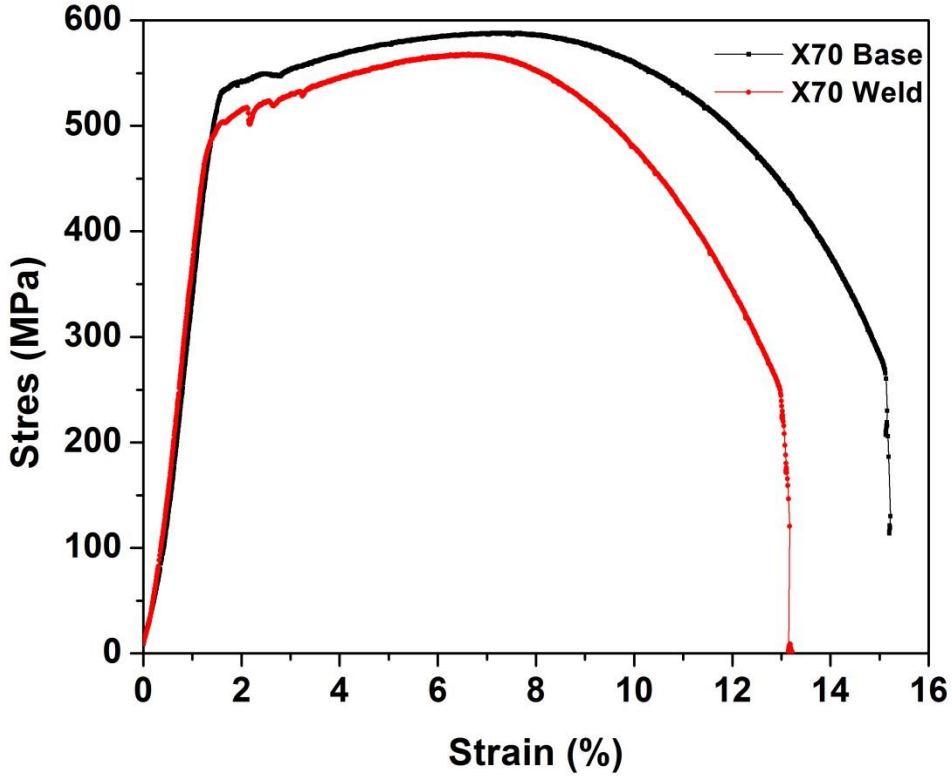

Figure 19. Stress strain curves for X70 base and weld metals

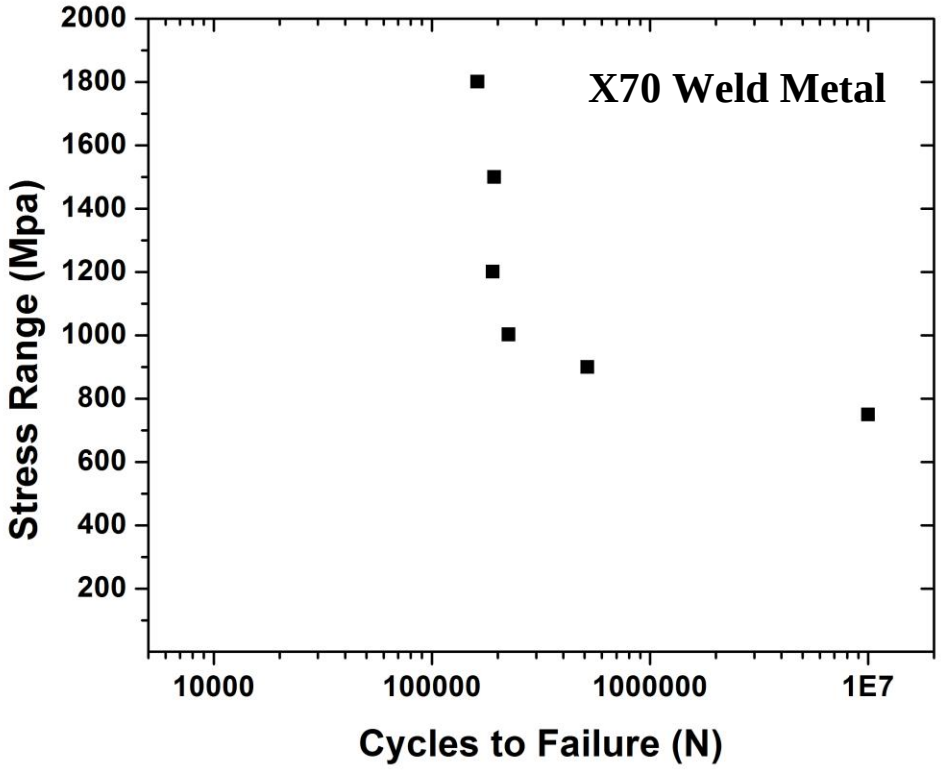

Figure 20 Stress versus cycles to failure for X70 weld four point bending fatigue samples

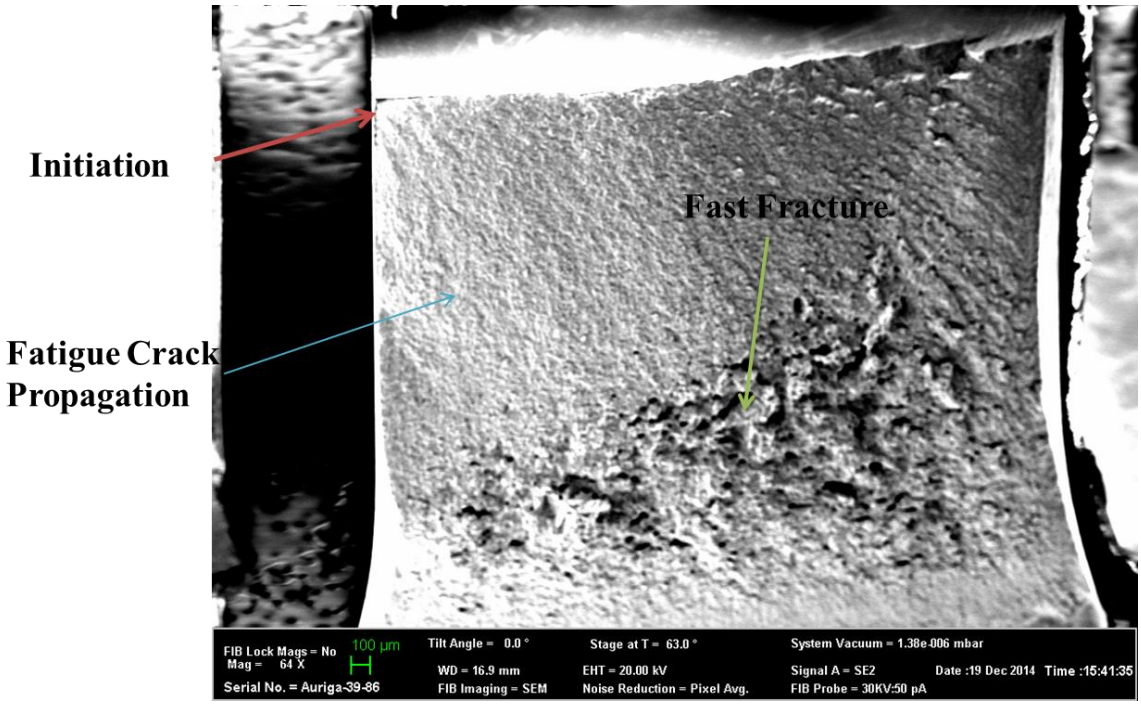

Figure 21. Fracture surface of an X70 weld four point bending fatigue sample (whole region)

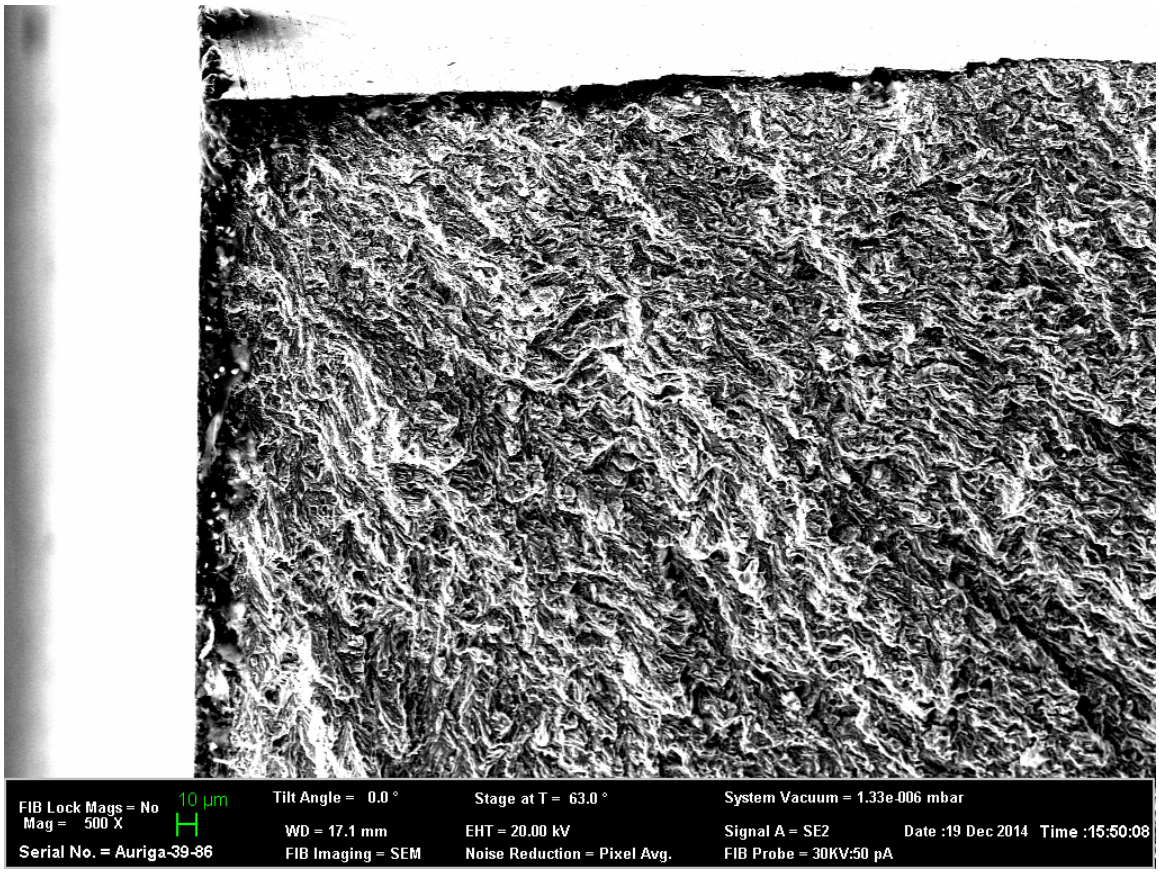

Figure 22. Fracture surface of an X70 weld four point bending fatigue sample (crack initiation and growth regions)

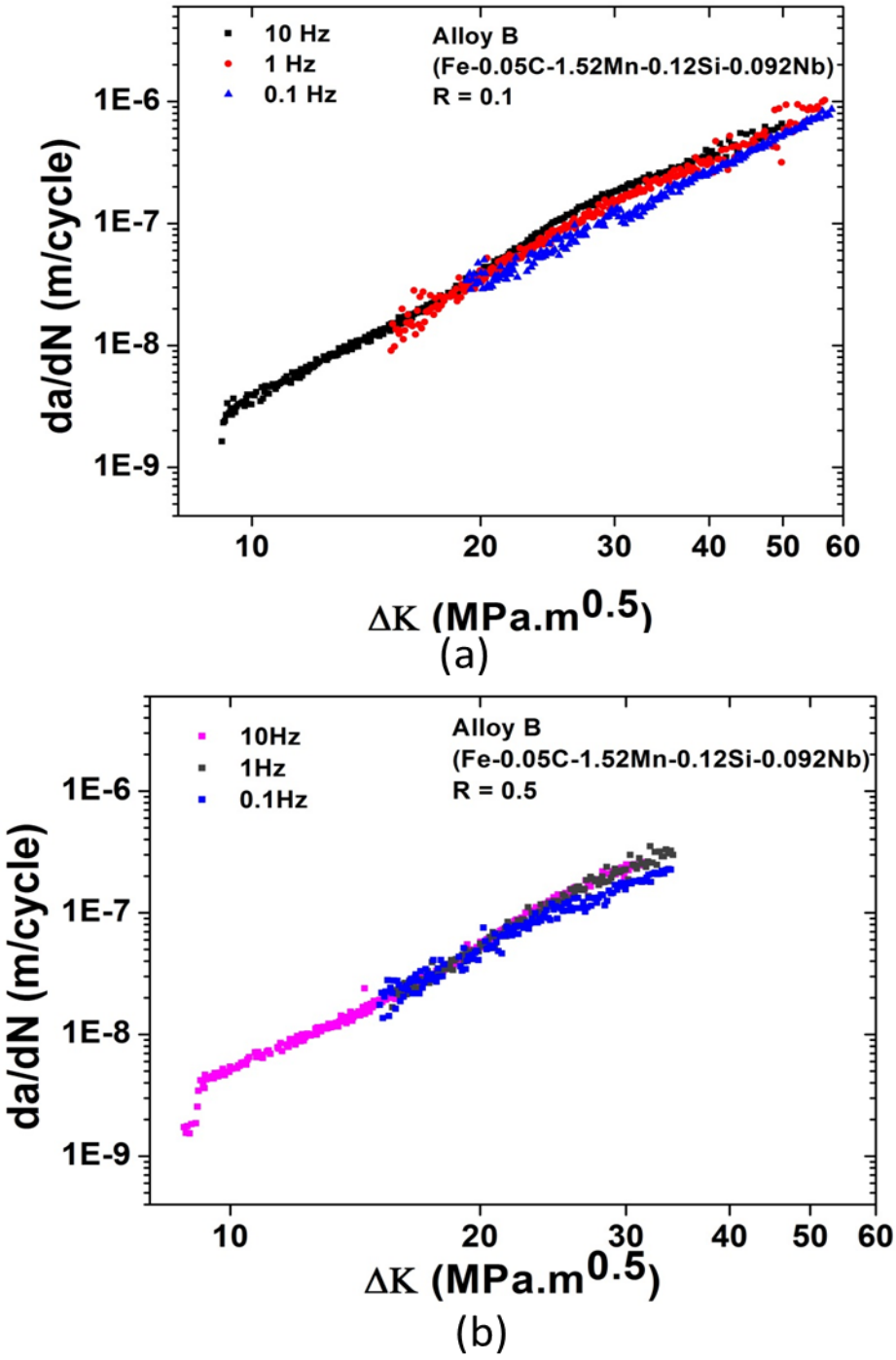

Figure 23. FCGR (da/dN) versus stress-intensity-factor range (ΔK) for Alloy B at different frequencies (0.1, 1 and 10 Hz). (a) R = 0.1 and (b) R = 0.5

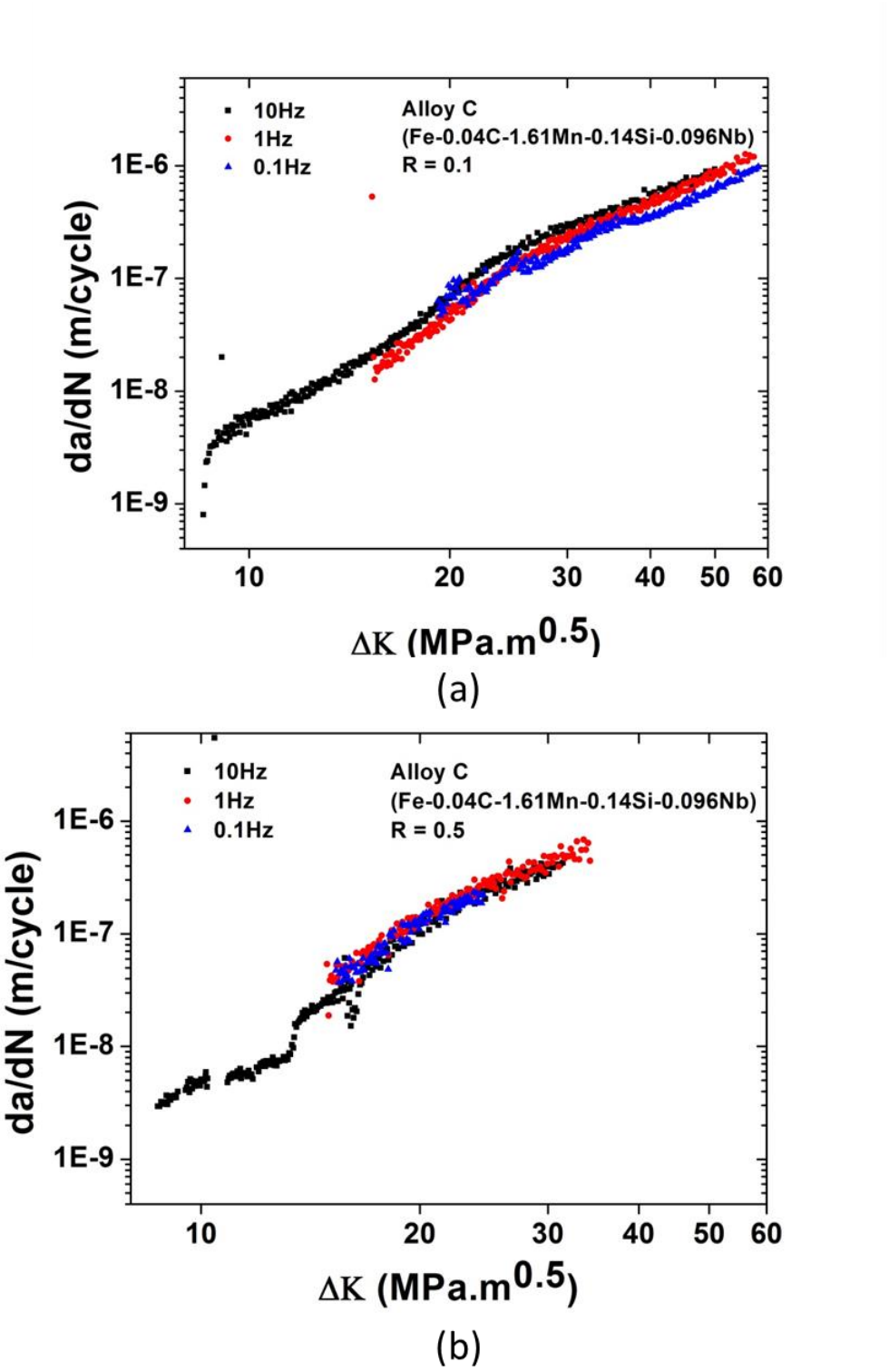

Figure 24. FCGR (da/dN) versus stress-intensity-factor range (ΔK) for Alloy C at different frequencies (0.1, 1, and 10 Hz. (a) R=0.1 and (b) R=0.5

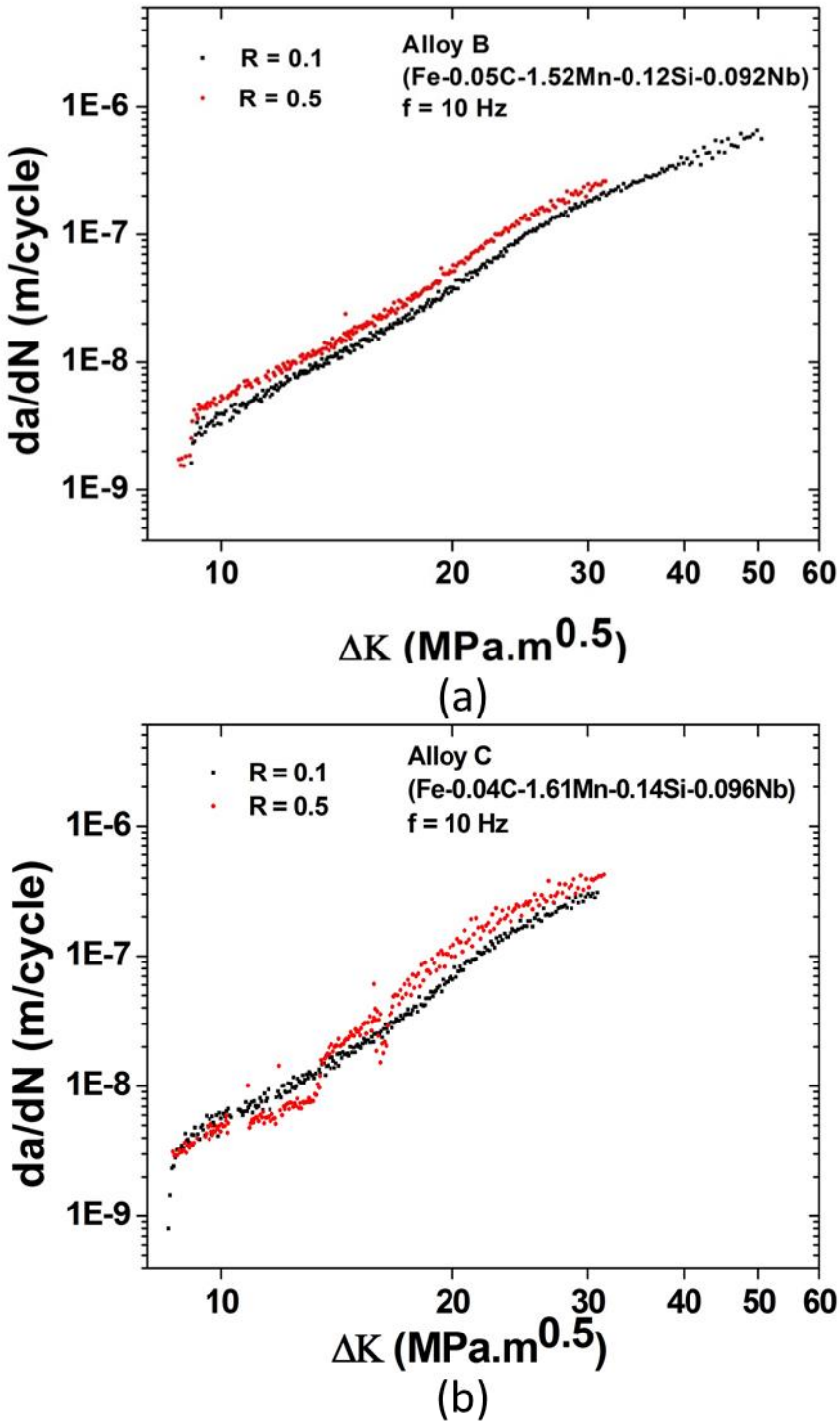

Figure 25. FCGR (da/dN) versus stress-intensity-factor range (ΔK) for different stress ratios at 10 Hz. (a) Alloy B and (b) Alloy C

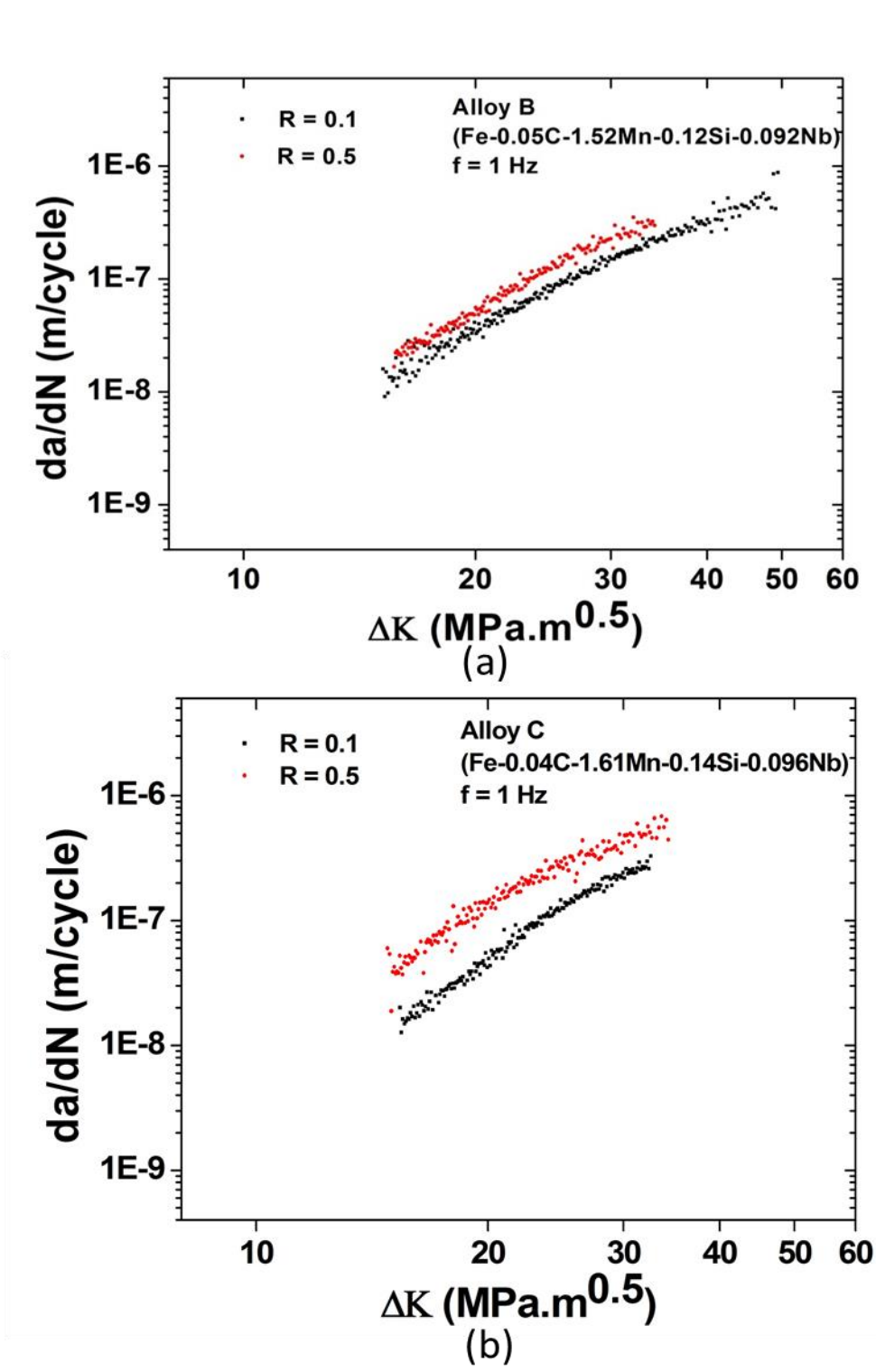

Figure 26. FCGR (da/dN) versus stress-intensity-factor range (ΔK) for different stress ratios at 1 Hz. (a) Alloy B and (b) Alloy C

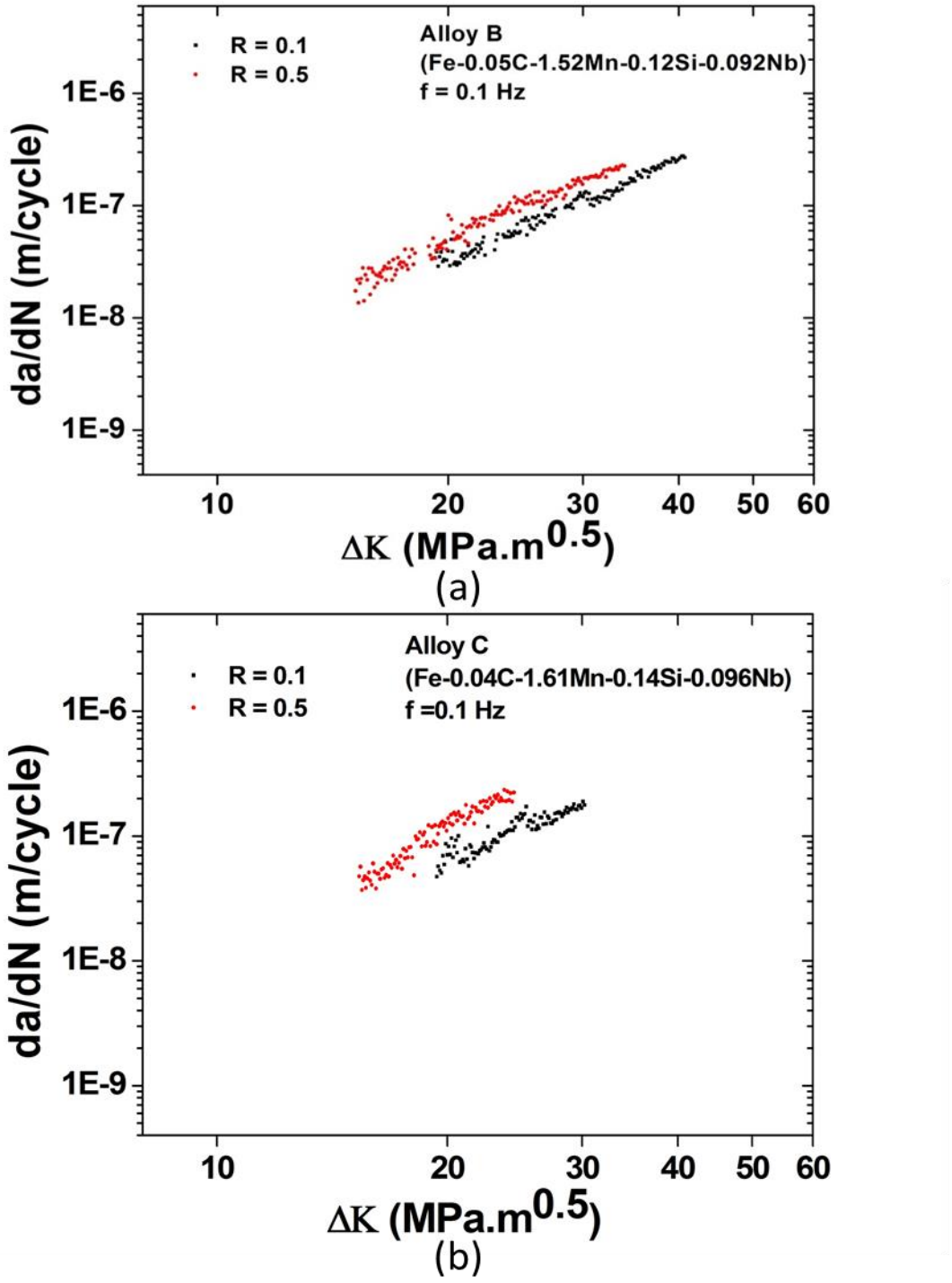

Figure 27. FCGR (da/dN) versus stress-intensity-factor range (ΔK) for different stress ratios at 0.1 Hz. (a) Alloy B and (b) Alloy C

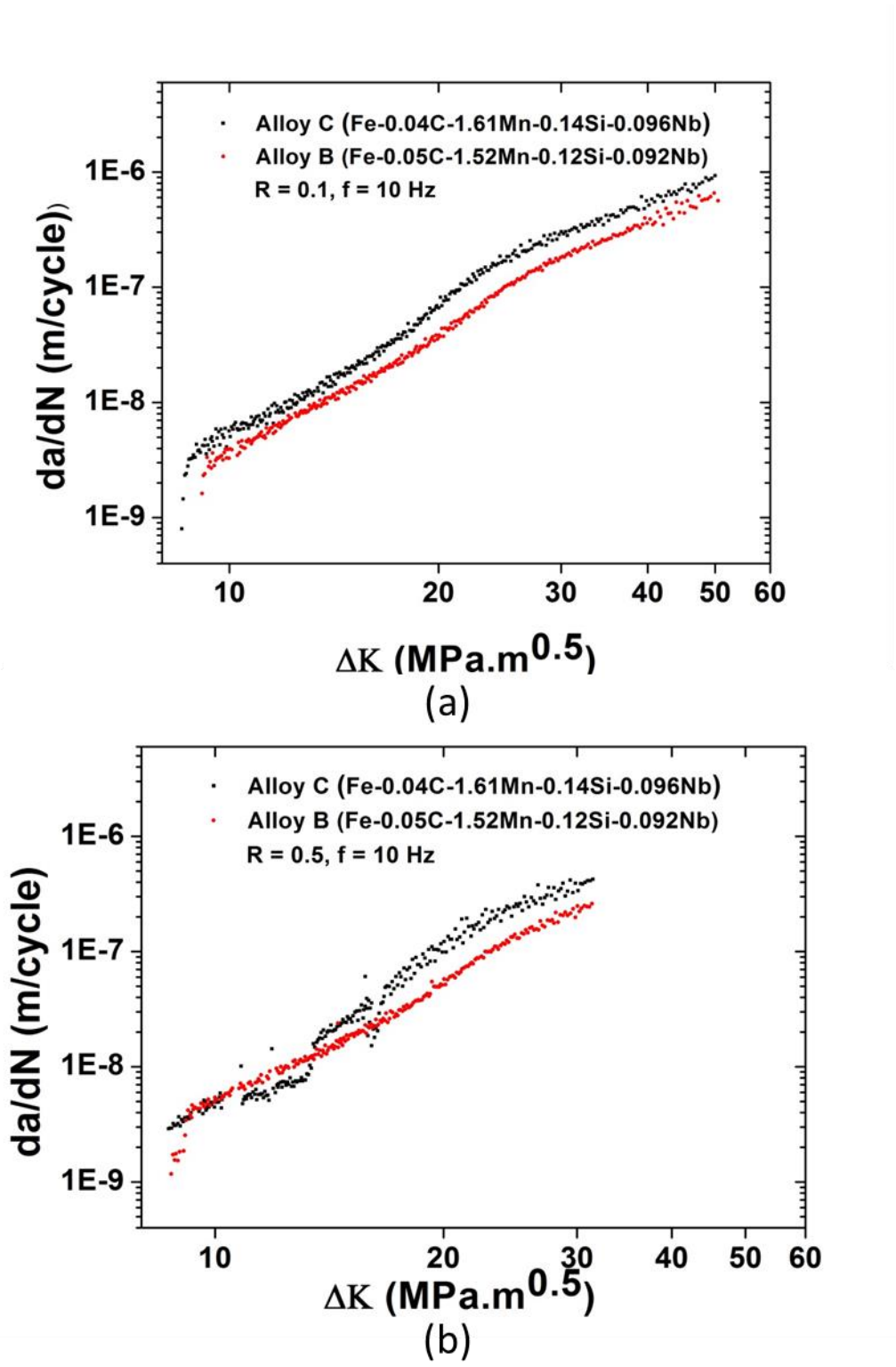

Figure 28. Comparison of FCGR curves for Alloys B and C at 10 Hz with (a) R = 0.1 and (b) R = 0.5

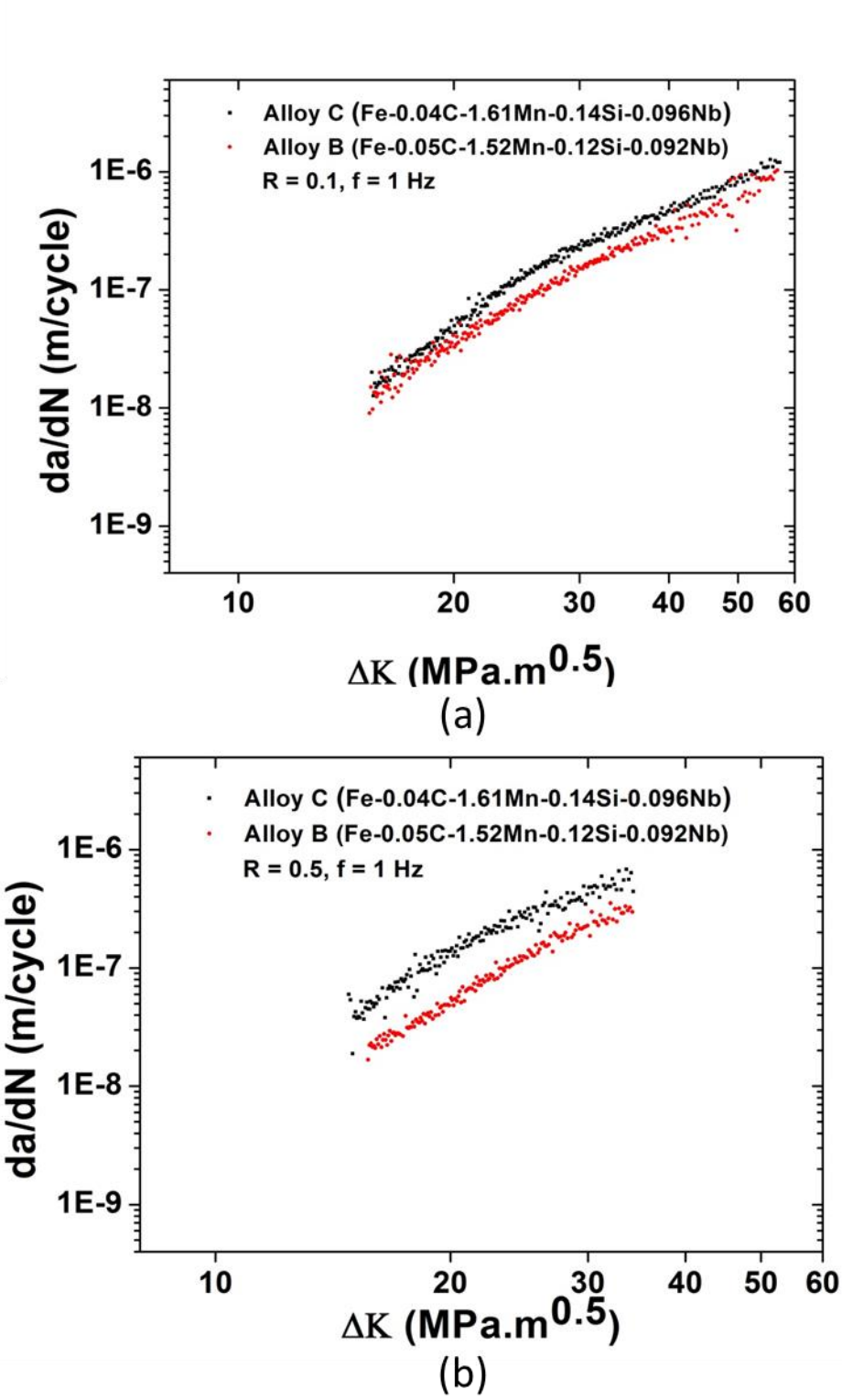

Figure 29. Comparison of FCGR curves for Alloys B and C at 1 Hz with (a) R = 0.1 and (b) R = 0.5

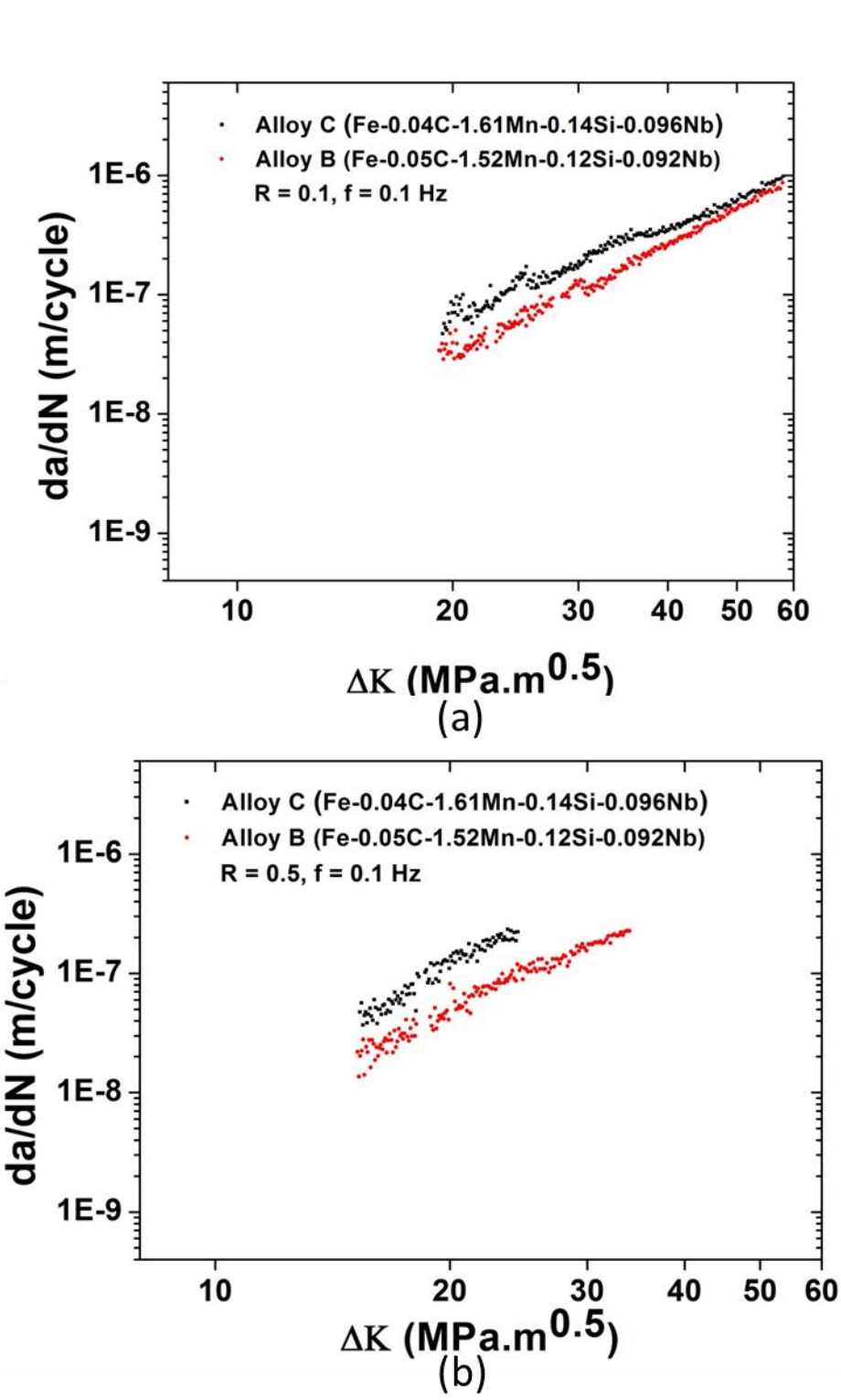

Figure 30. Comparison of FCGR curves for Alloys B and C at 0.1 Hz with (a) R = 0.1 and (b) R = 0.5

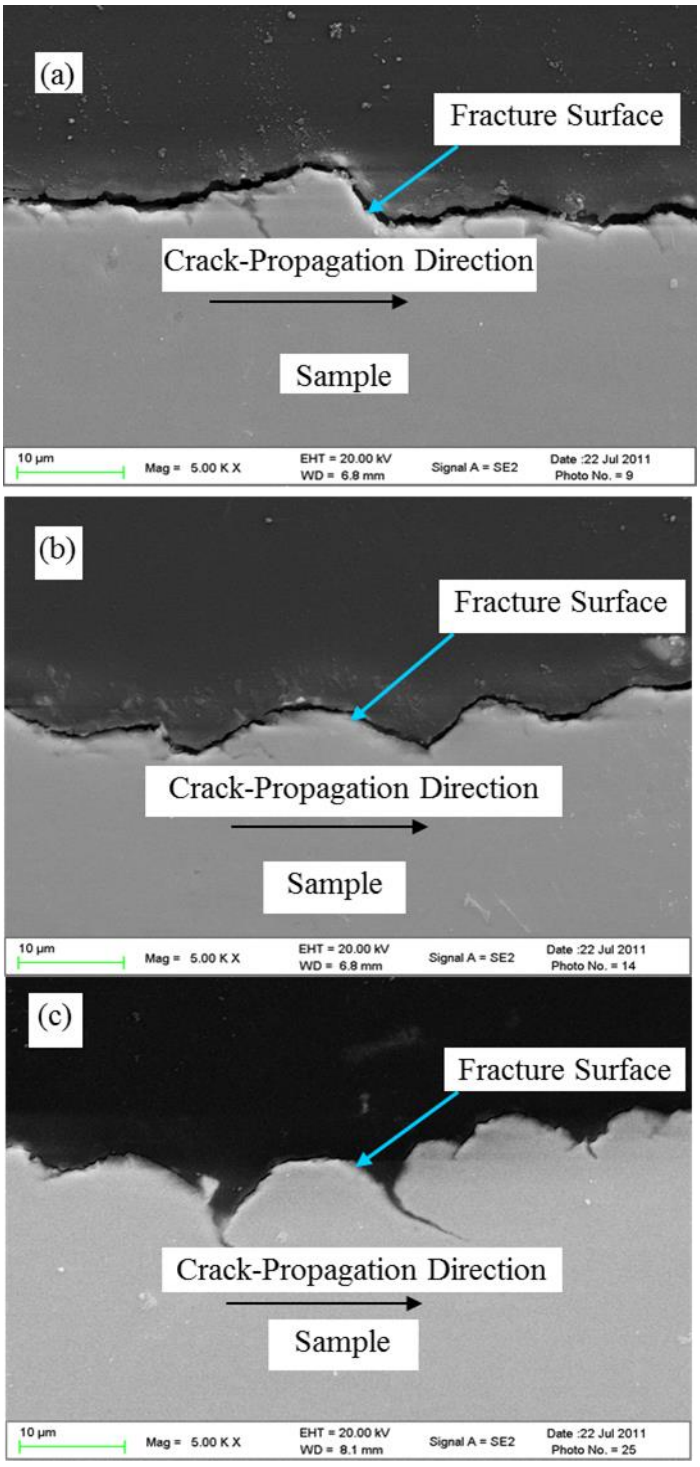

Figure 31. The side view fracture morphology of the fatigued Alloy C at a frequency of 10 Hz in the different ΔK range: (a) ΔK = 10 MPa.m$^{0.5}$, (b) ΔK = 25 MPa.m$^{0.5}$, and (c) ΔK = 40 MPa.m$^{0.5}$.

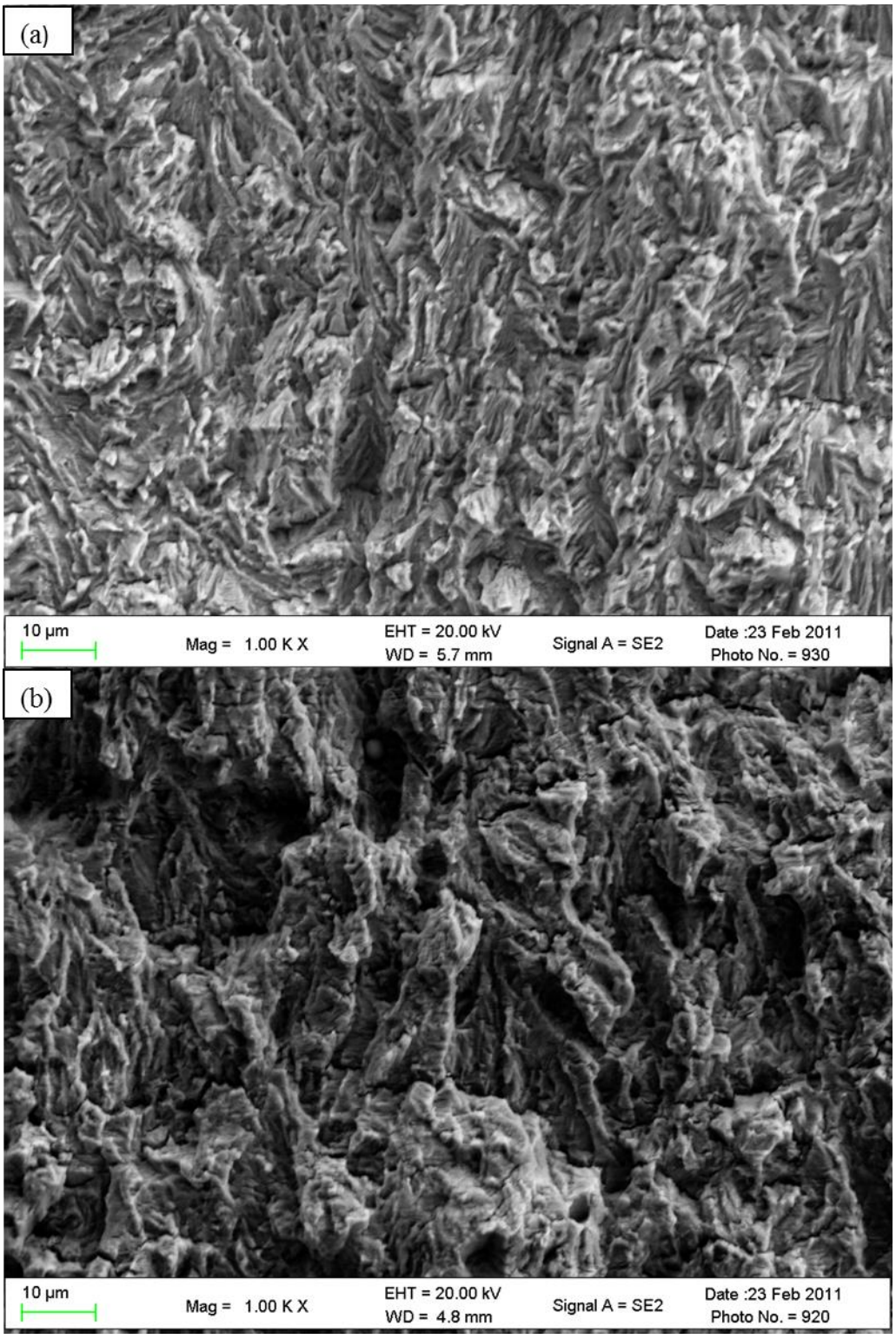

Figure 32. SEM images of fracture surfaces at ΔK = 10 MPa.m$^{0.5}$, (a) Alloy B and (b) Alloy C.

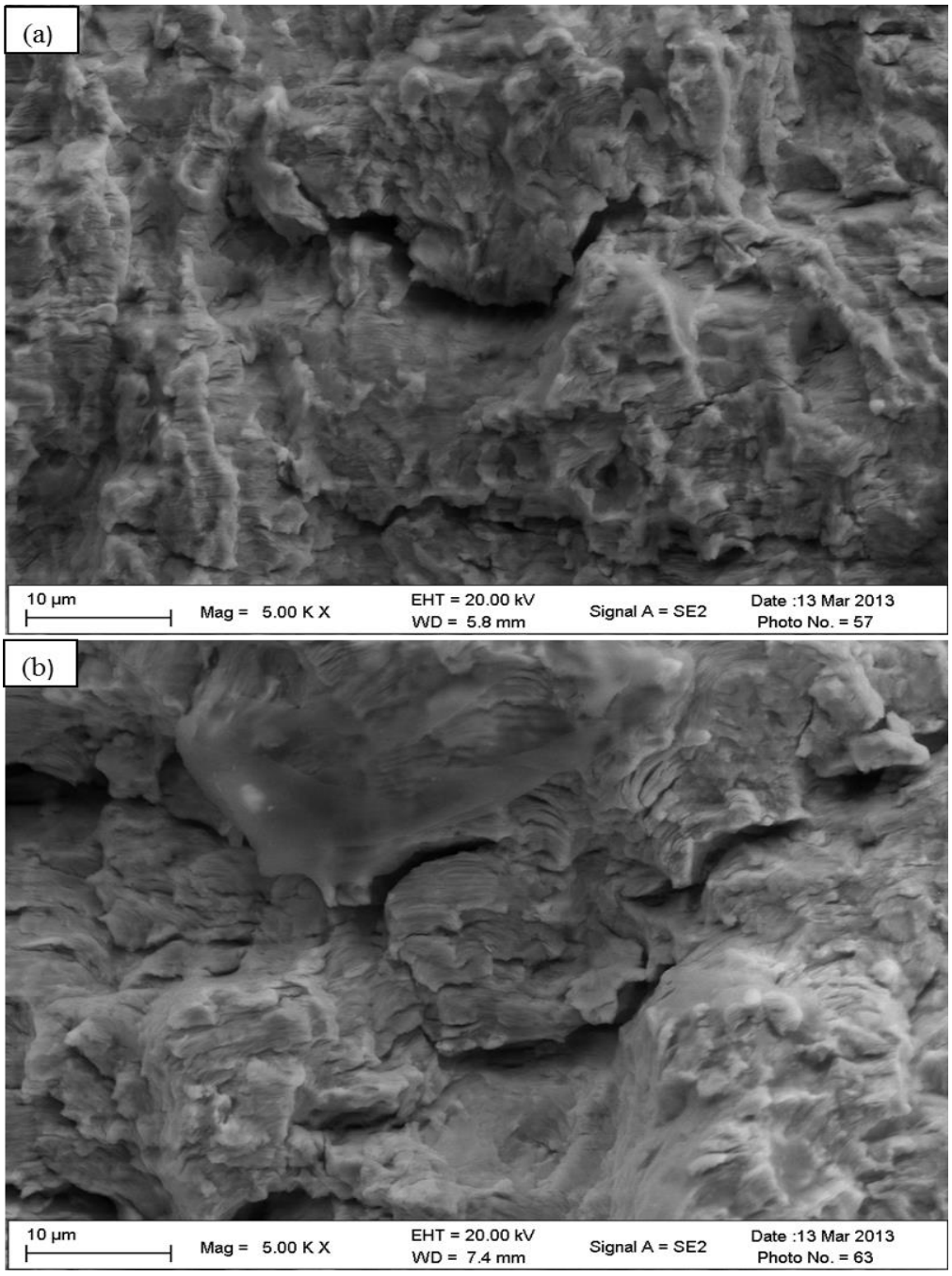

Figure 33. SEM images of fracture surface of Alloy B (a) ΔK = 30 MPa.m$^{0.5}$and (b) ΔK = 45 MPa.m$^{0.5}$

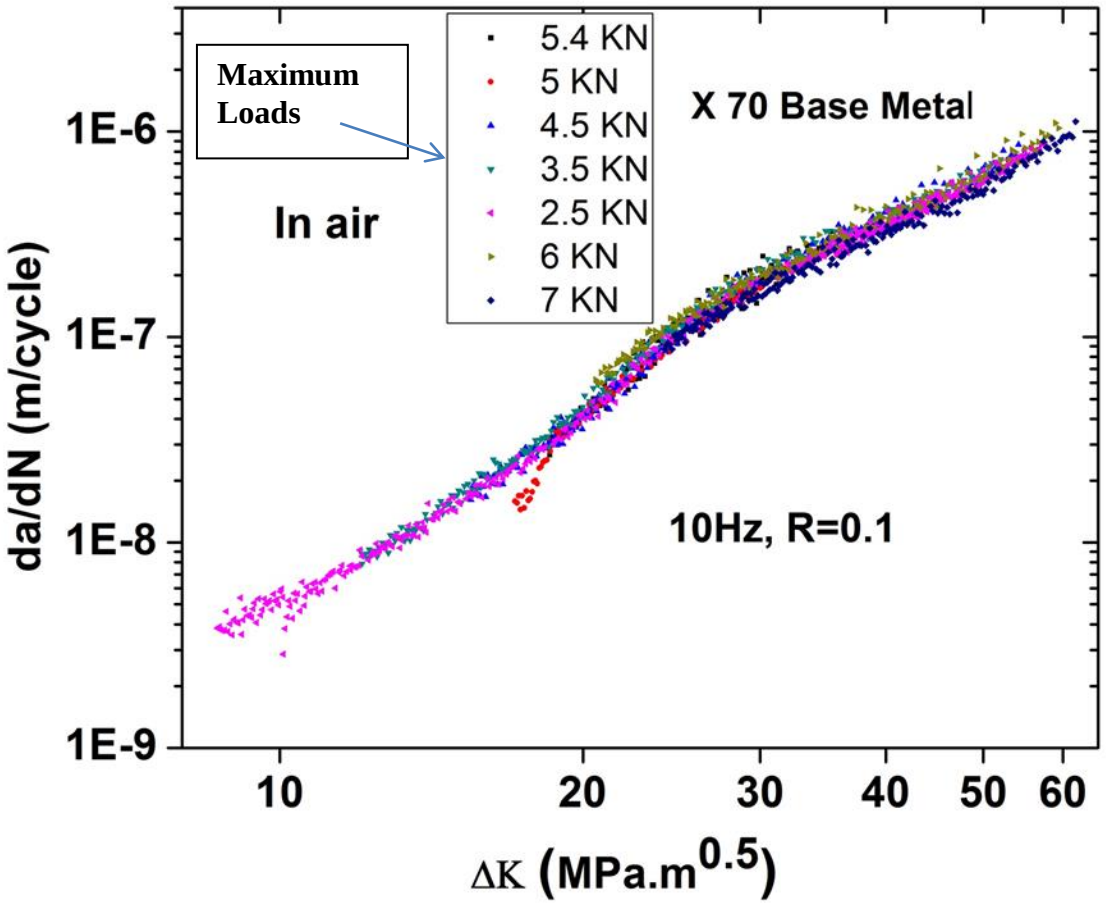

Figure 34. FCGR (da/dN) versus stress-intensity-factor range (ΔK) for the X70 base metal at different load levels

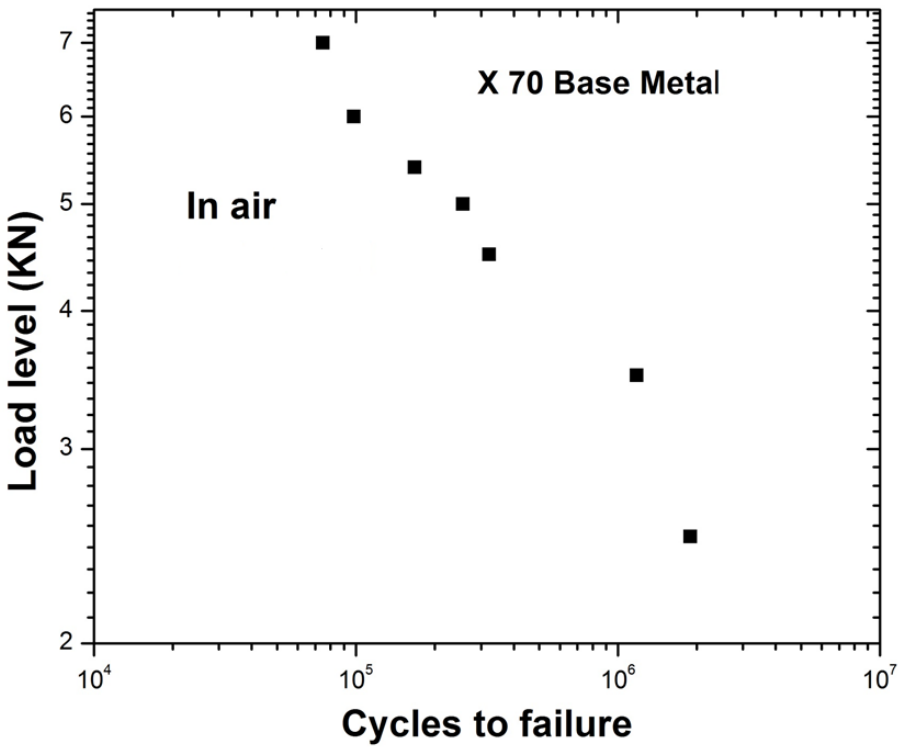

Figure 35. Load level versus cycles to failure for X70 base metal when R = 0.1 and f = 10 Hz

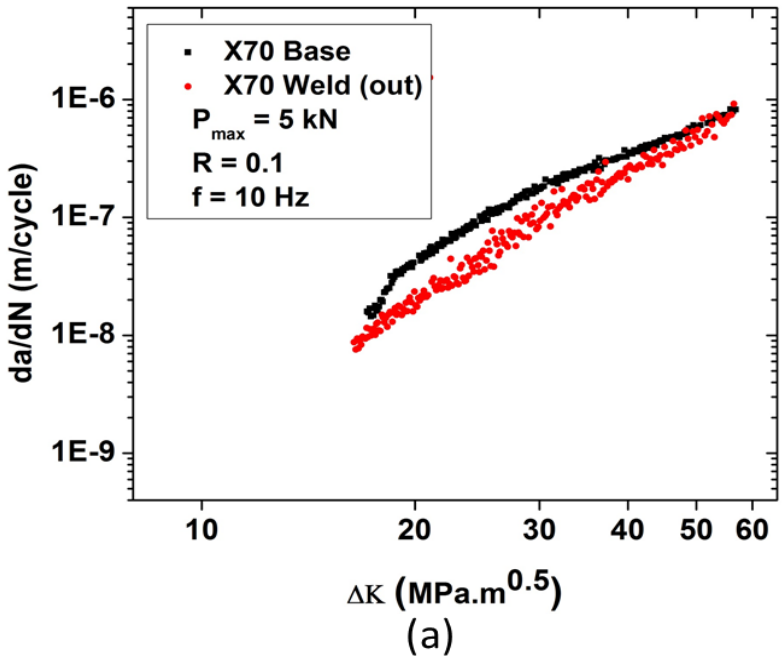

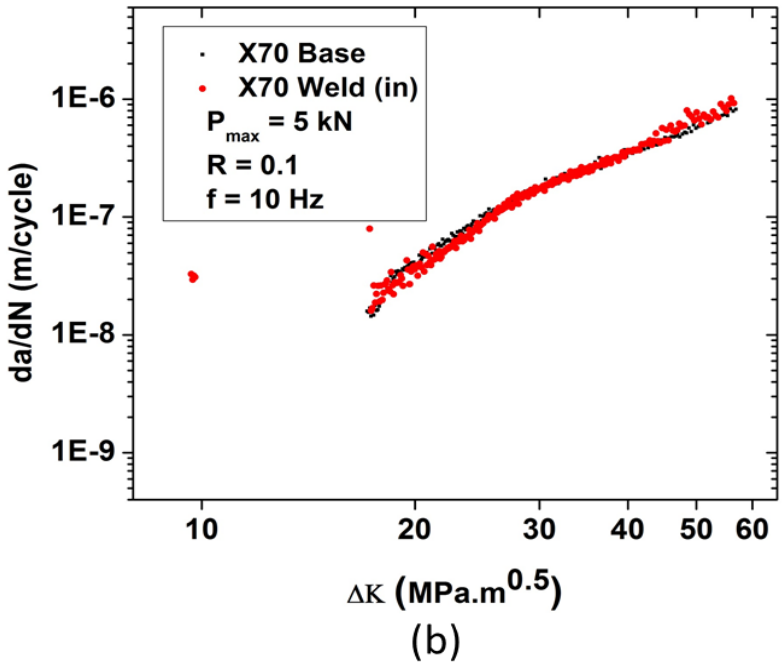

Figure 36. Comparison of FCGR curves of (a) X70 base and upper weld (b) X70 base and lower weld when Pmax = 5 kN, R = 0.1 and f = 10 Hz

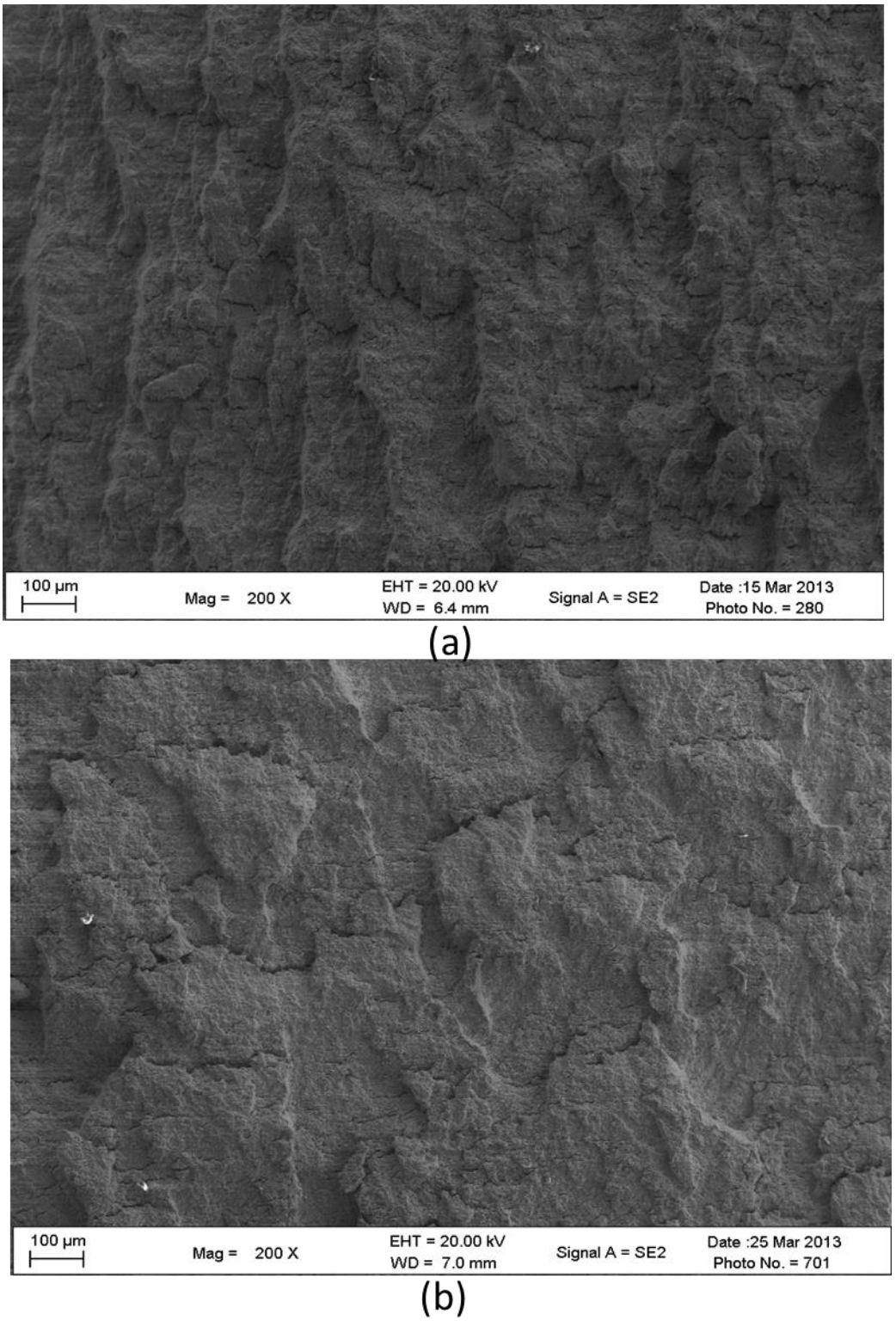

Figure 37. SEM image of fracture surface (ΔK = 40 MPa.m$^{0.5}$), (a) X70 base (2) X70 weld

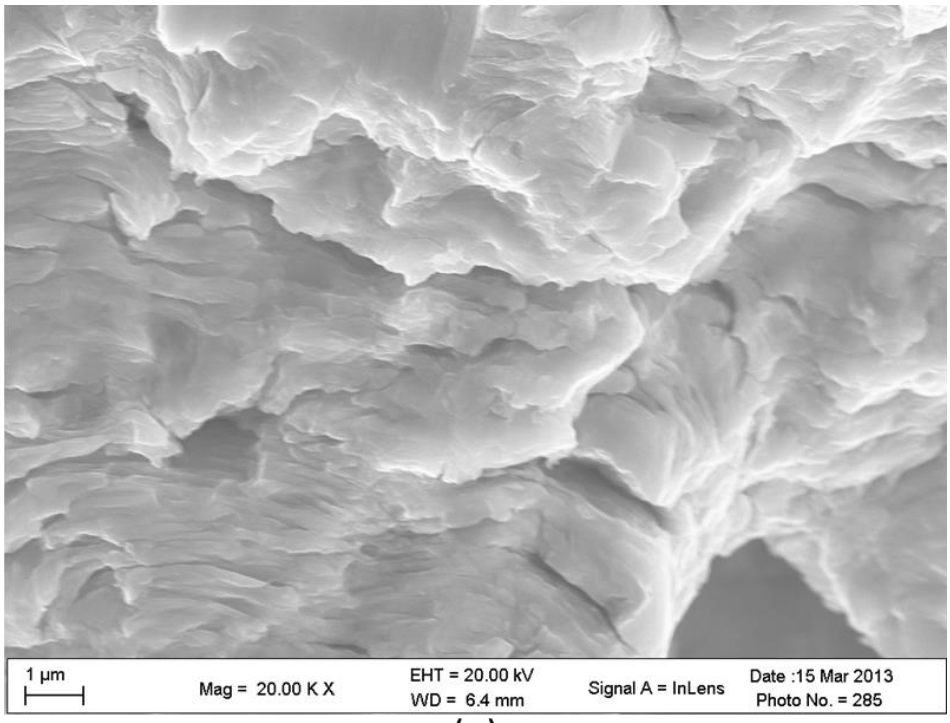

(a)

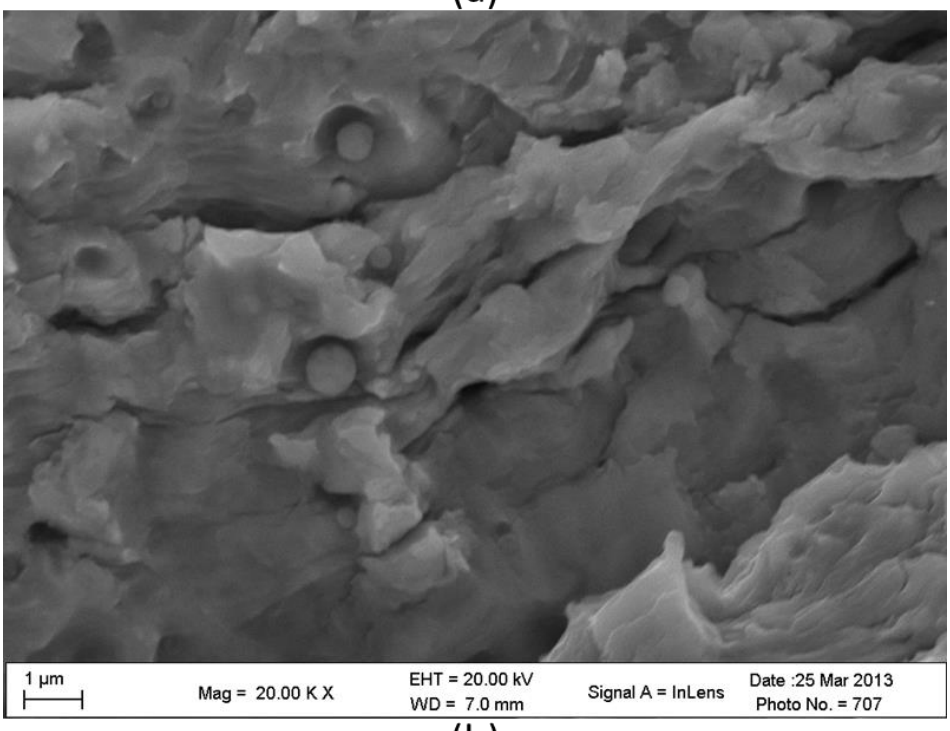

(b)

Figure 38. SEM image of fracture surface at high magnification. (a) X70 base and (b) X70 weld

Figure 39 Spallation Neutron Source (SNS) at ORNL

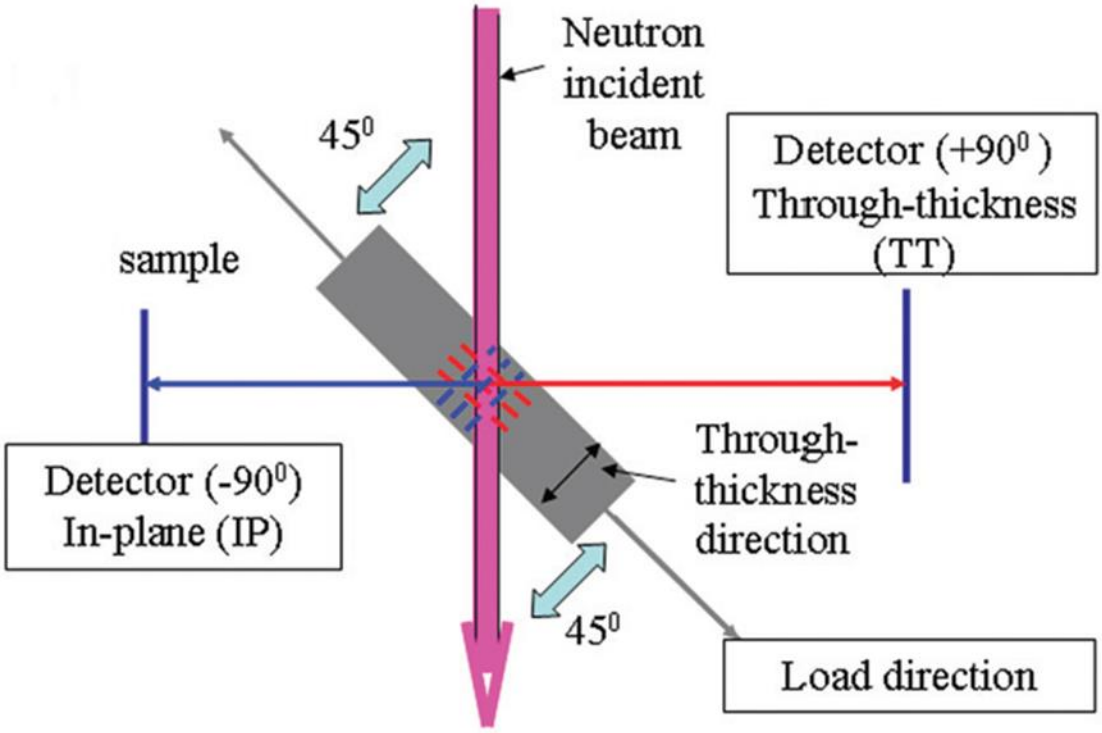

Figure 40. Sketch of the neutron-diffraction geometry of the experiments

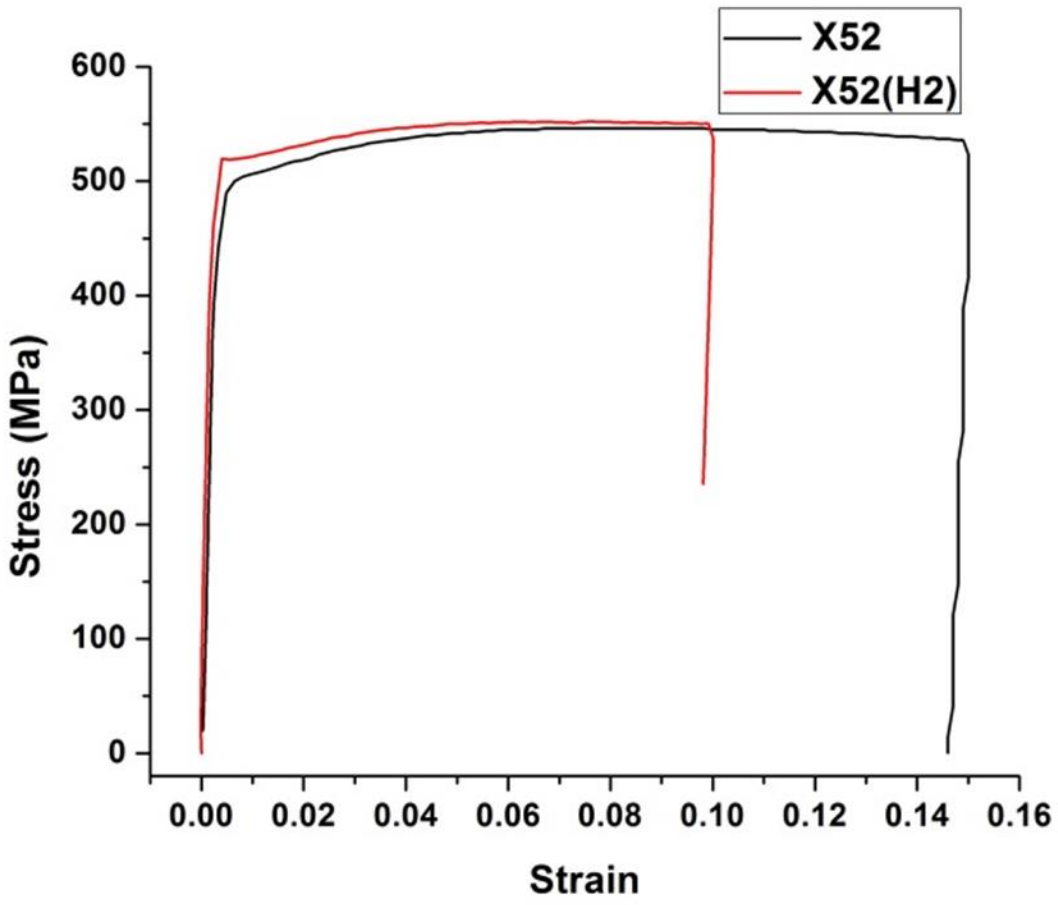

Figure 41. Stress versus strain for X52 samples with and without hydrogen charge

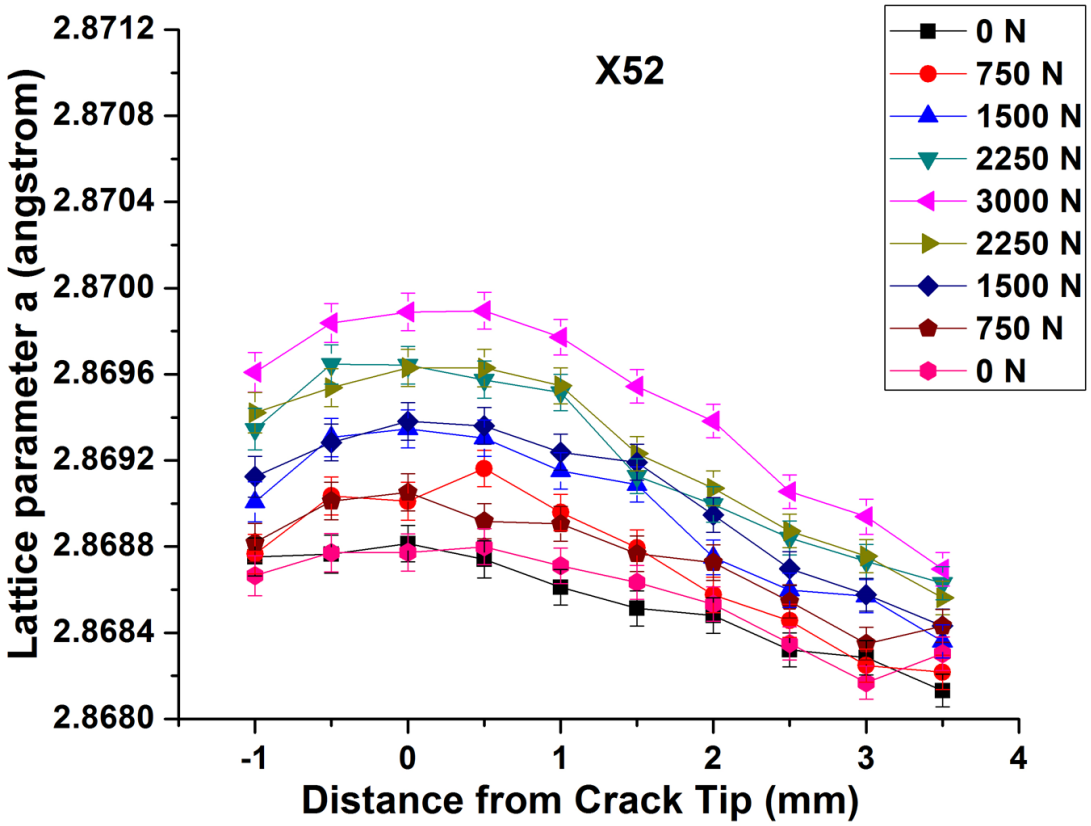

Figure 42. Lattice parameter as a function of the distance from the crack tip in the X52 original sample

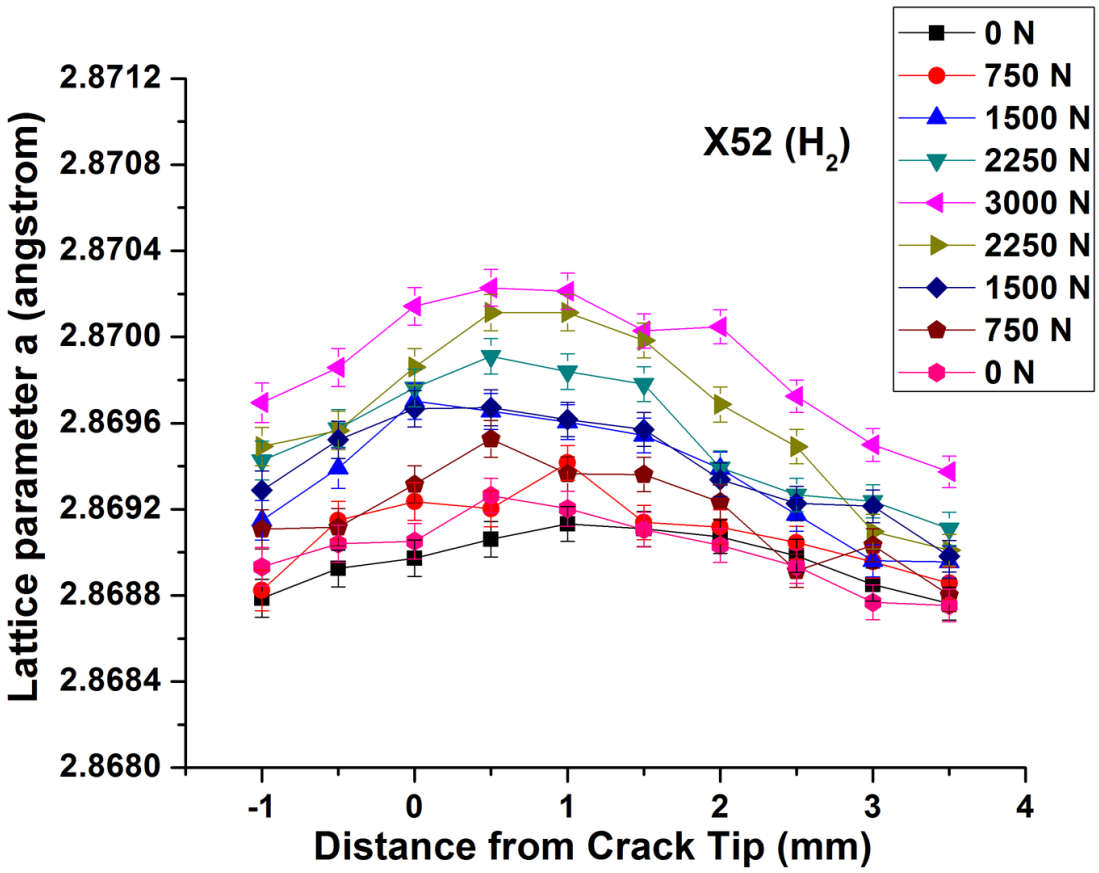

Figure 43. Lattice parameter as a function of the distance from the crack tip in the X52 hydrogen-charged sample

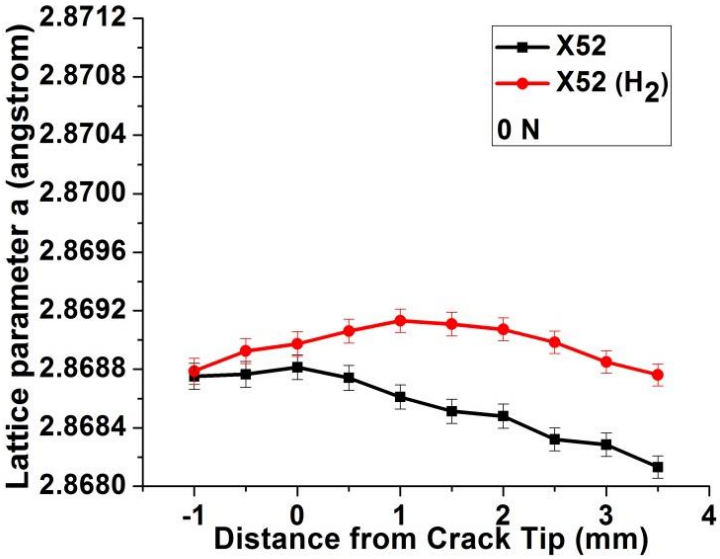

(a)

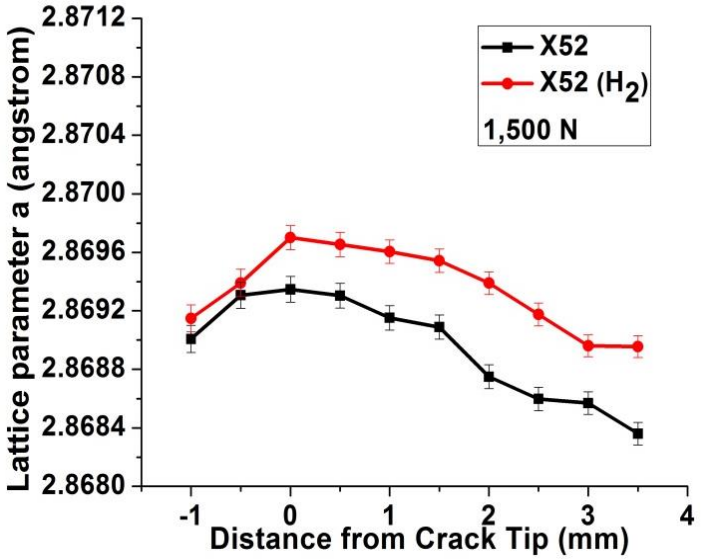

(b)

Figure 44 Loading

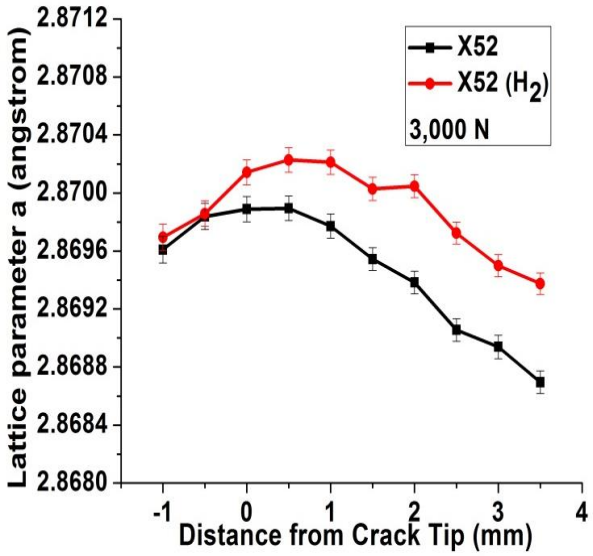

(c)

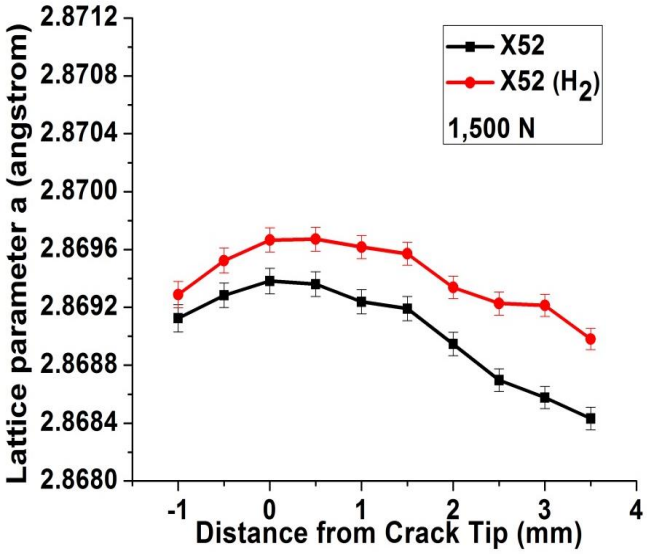

(d)

Figure 44. Unloading

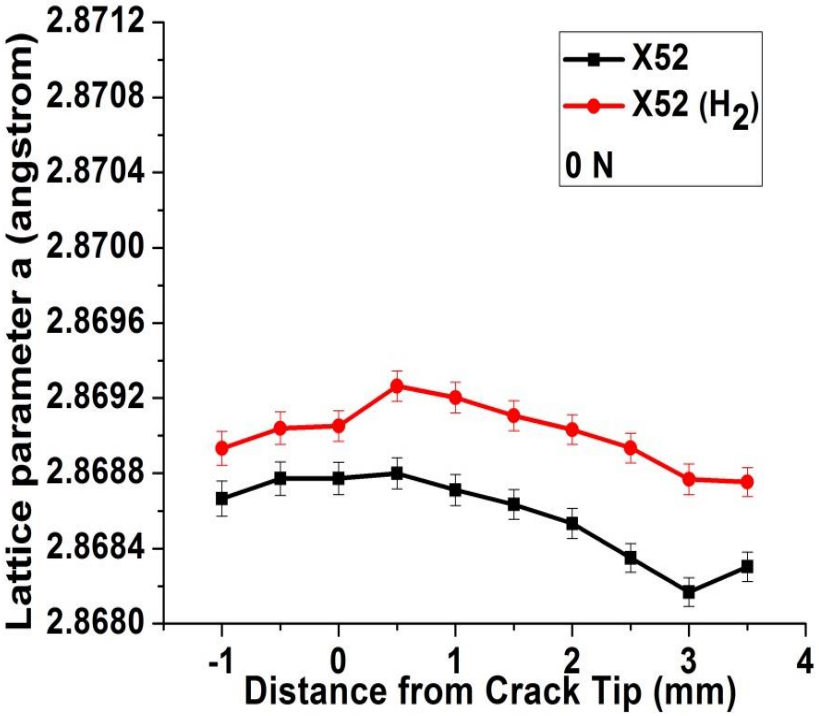

(f)

Figure 44. Lattice parameter of X52 samples as a function of distance from crack tip during one loading-unloading cycle

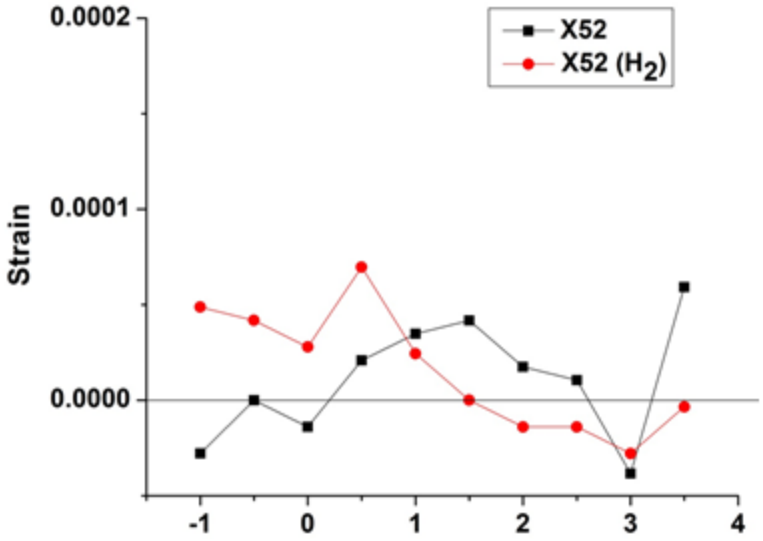

Figure 45. Lattice strain versus distance from crack tip after one cycle (X52)

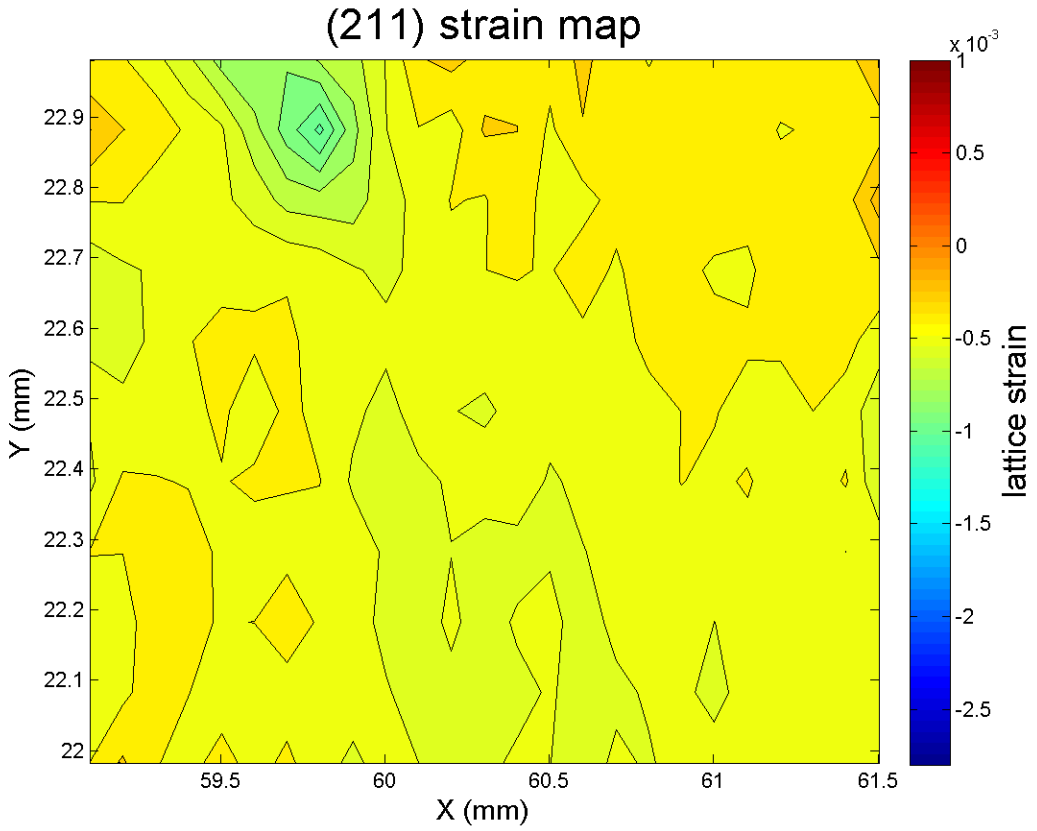

Figure 46. (211) strain map around the fatigue crack tip for precracked Alloy C before loading

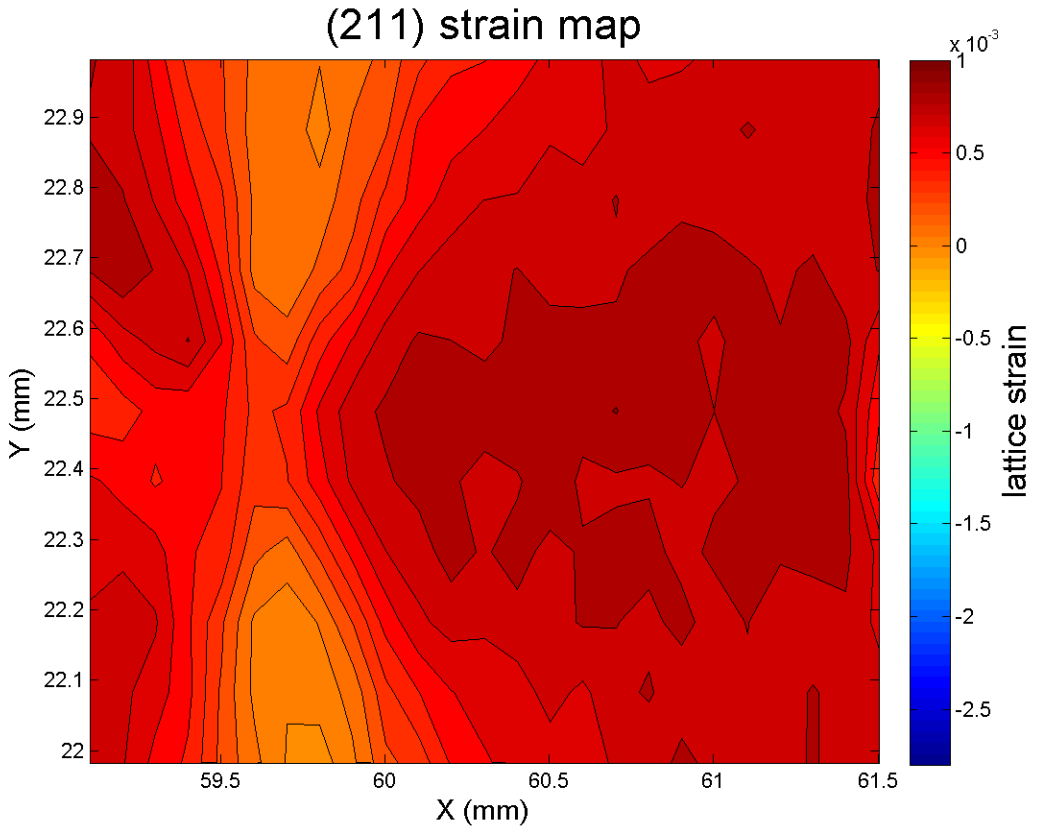

Figure 47. (211) strain map around the fatigue crack tip for precracked Alloy C when 3000 N was applied

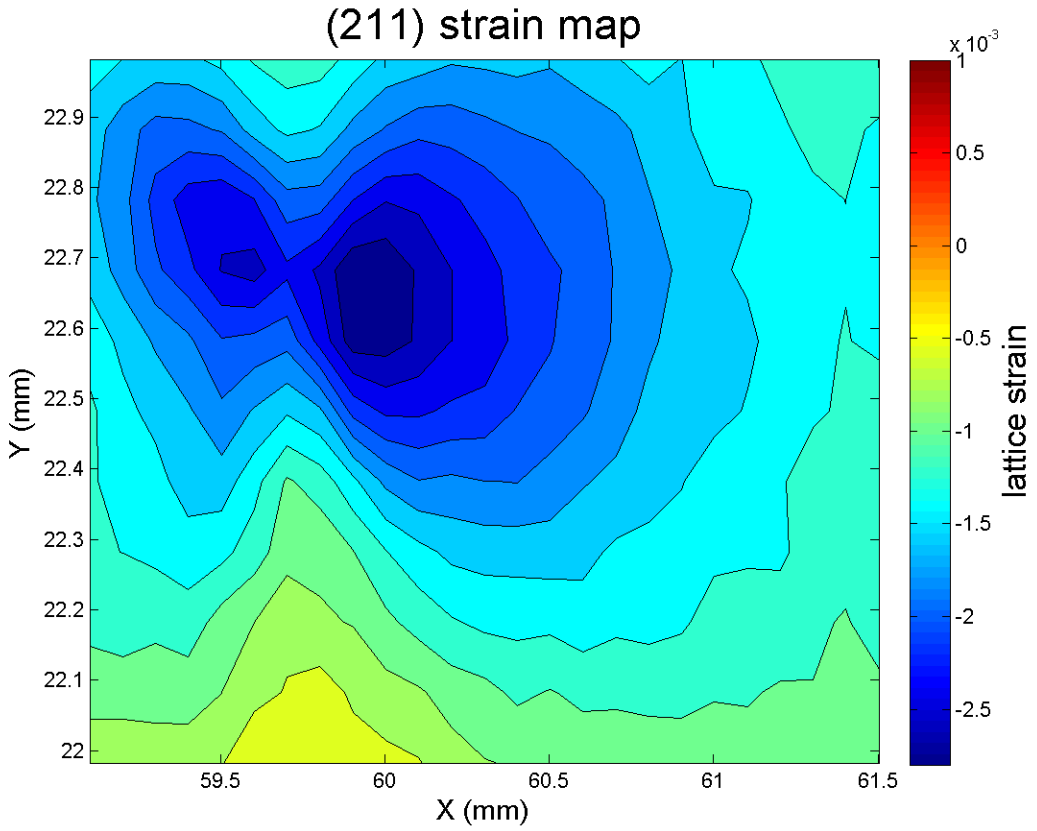

Figure 48. (211) strain map around the fatigue crack tip for precracked Alloy C right after a loading-unloading cycle

D. ACKNOWLEDGEMENTS

We genuinely appreciate the following persons for their support and encouragement.

(1) Jim Merritt, U.S. Department of Transportation Federal Aviation, under Grant No. USDOTDTPH56-10-T-000001.

(2) David Clarke, Doug Fielden, Carol Hatmaker, and Tammy Enix, The University of Tennessee, Knoxville.

(3) Zhili Feng, Yanli Wang, Ke An, David Stinton, and Steven Pawel, Oak Ridge National Laboratory (ORNL).

(4) Andy Slifka and Elizabeth Drexler, National Institute of Standards and Technology (NIST).

(5) Wei Zhang, Ohio State University (OSU).

(6) Louis Hayden, Louis E. Hayden Associates.

(7) Doug Stalheim, DGS Metallurgical Solutions, Inc.

(8) Yang Ren, Argonne National Laboratory.

E. REFERENCES

[1] Greiner CJ, KorpÅs M, Holen AT. A Norwegian case study on the production of hydrogen from wind power. International Journal of Hydrogen Energy 2007;32:1500.

[2] Leighty W, Holloway J, Merer R, Somerday B, San Marchi C, Keith G, White D, Economics SE. Compressorless hydrogen transmission pipelines deliver large-scale stranded renewable energy at competitive cost. Proceedings of the 16th World Hydrogen Energy Conference, Lyon, FR, June, vol. 6, 2006.

[3] Mohitpour M, Golshan H, Murray A. Natural Gas Transmission: ASME press, 2007.

[4] Nanninga N, Slifka A, Levy Y, White C. A review of fatigue crack growth for pipeline steels exposed to hydrogen. Journal of Research of the National Institute of Standards and Technology 2010;115:437.

[5] Patel MR. Wind and solar power systems: design, analysis, and operation: CRC press, 2012.

[6] Dahlberg EP, and Bruno TV. Analysis of gas pipeline failure. 1990.

[7] Schmidt JT. Pipeline integrity management. API Inspection Summit and Expo, 2011.

[8] Baker M, Ressler R. Pipeline Corrosion. Pipeline and Hazardous Materials Safety Administration, 2008.

[9] Fang B, Atrens A, Wang J, Han E-H, Zhu Z, Ke W. Review of stress corrosion cracking of pipeline steels in "low" and "high" pH solutions. Journal of Materials Science 2003;38:127.

[10] Pao P. Mechanisms of corrosion fatigue. ASM International, Member/Customer Service Center, Materials Park, OH 44073-0002, USA, 1996:185.

[11] Parkins RN. A review of stress corrosion cracking of high pressure gas pipelines. Corrosion 2000.

[12] Wang G, Liaw P, Peker A, Yang B, Benson M, Yuan W, Peter W, Huang L, Freels M, Buchanan R. Fatigue behavior of Zr–Ti–Ni–Cu–Be bulk-metallic glasses. Intermetallics 2005;13:429.

[13] Shanmugam S, Misra R, Hartmann J, Jansto S. Microstructure of high strength niobium-containing pipeline steel. Materials Science and Engineering: A 2006;441:215.

[14] Wang W, Yan W, Zhu L, Hu P, Shan Y, Yang K. Relation among rolling parameters, microstructures and mechanical properties in an acicular ferrite pipeline steel. Mater. Des. 2009;30:3436.

[15] Xiao F, Liao B, Ren D, Shan Y, Yang K. Acicular ferritic microstructure of a low-carbon Mn–Mo–Nb microalloyed pipeline steel. Materials Characterization 2005;54:305.

[16] Zhao M-C, Yang K, Shan Y. The effects of thermo-mechanical control process on microstructures and mechanical properties of a commercial pipeline steel. Materials Science and Engineering: A 2002;335:14.

[17] Stalheim D, Boggess T, San Marchi C, Jansto S, Somerday B, Muralidharan G, Sofronis P. Microstructure and mechanical property performance of commercial grade API pipeline steels in high pressure gaseous hydrogen. 2010 8th International Pipeline Conference: American Society of Mechanical Engineers, 2010. p.529.

[18] Bruno T. How to Prevent Fatigue to Tubular Goods. Standardization Conference for the Production Department, American Petroleum Institute, New Orleans, LA, 1987.

[19] Jaske CE. The Effect of Cathodic Polarization on Fatigue Behavior. CORROSION 2003 2003.

[20] Kunert H, Otegui J. Factors influencing transit fatigue of seamless pipes. Fatigue & Fracture of Engineering Materials & Structures 2005;28:455.

[21] Chu R, Chen W, Wang S-H, King F, Jack T, Fessler R. Microstructure dependence of stress corrosion cracking initiation in X-65 pipeline steel exposed to a near-neutral pH soil environment. CORROSION 2004;60:275.
[22] Cialone H, Holbrook J. Effects of gaseous hydrogen on fatigue crack growth in pipeline steel. Metallurgical Transactions A 1985;16:115.
[23] Shi Y, Chen B, Zhang J. Effects of welding residual stresses on fatigue crack growth behaviour in butt welds of a pipeline steel. Engineering Fracture Mechanics 1990;36:893.
[24] Vosikovsky O. Effects of stress ratio on fatigue crack growth-rates in X70 pipeline steel in air and saltwater. Journal of Testing and Evaluation 1980;8:68.
[25] Anderson TL. Fracture mechanics: fundamentals and applications: CRC press, 2005.
[26] Suresh S. Fatigue of materials: Cambridge university press, 1998.
[27] Hopkins P. Oil and Gas Pipelines: Yesterday and Today. Pipeline Systems Division (PSD), International Petroleum Technology Institute, American Society of Mechanical Engineers (ASME). Available online at http://www. engr. mun. ca/~ spkenny/Courses/Undergraduate/ENGI8673/Reading_List/2007_Hopkins. pdf 2007.
[28] Lam P, Sindelar R, Duncan A, Adams T. Literature survey of gaseous hydrogen effects on the mechanical properties of carbon and low alloy steels. Journal of Pressure Vessel Technology 2009;131:041408.
[29] Lee S, Choo H, Liaw PK, An K, Hubbard CR. A study on fatigue crack growth behavior subjected to a single tensile overload: Part II. Transfer of stress concentration and its role in overload-induced transient crack growth. Acta Materialia 2011;59:495.
[30] Lee SY. Effects of Overload and Underload on Internal Strains/Stresses and Crack Closure during Fatigue-Crack Propagation. 2009.
[31] Birnbaum H. Hydrogen effects on deformation and fracture: science and sociology. MRS bulletin 2003;28:479.
[32] Liaw P, Leax T, Donald J. Fatigue crack growth behavior of 4340 steels. Acta Metallurgica 1987;35:1415.
[33] Liaw P, Leax T, Fabis T, Donald J. Fatigue crack growth behavior in an Mn-Cr austenitic steel. Engineering Fracture Mechanics 1987;26:1.
[34] ASTM Standard E647-99: Standard test method for measurement of fatigue crack-growth rates. Annual Book of ASTM Standards, vol. 03.01, 2000. p. 591.
[35] Bain EC. Functions of the alloying elements in steel: American Society for Metals, 1939.
[36] Dowling N, Calhoun C, Arcari A. Mean stress effects in stress-life fatigue and the Walker equation. Fatigue & Fracture of Engineering Materials & Structures 2009;32:163.
[37] Rogante M, Battistella P, Rustichelli F. Residual stress measurement by neutron diffraction in AA6082 extruded samples submitted to different quenching rates. Journal of Alloys and Compounds 2004;378:335.
[38] Hossain S, Daymond M, Truman C, Smith D. Prediction and measurement of residual stresses in quenched stainless-steel spheres. Materials Science and Engineering: A 2004;373:339.
[39] Jung M, Kang M, Woo W, Lee Y-K. Evaluations of stress-free lattice spacings and residual stresses in a quenched carbon steel cylinder using neutron diffraction. Materials Science and Engineering: A 2013;565:392.
[40] Mark A, Francis J, Dai H, Turski M, Hurrell P, Bate S, Kornmeier J, Withers P. On the evolution of local material properties and residual stress in a three-pass SA508 steel weld. Acta Materialia 2012;60:3268.
[41] Pintschovius L, Jung V, Macherauch E, Vöhringer O. Residual stress measurements by means of neutron diffraction. Materials Science and Engineering 1983;61:43.

[42] Solanki K, Jordon J, Whittington W, Rao H, Hubbard C. Structure–property relationships and residual stress quantification of a friction stir spot welded magnesium alloy. Scripta Materialia 2012;66:797.
[43] Thibault D, Bocher P, Thomas M, Gharghouri M, Côté M. Residual stress characterization in low transformation temperature 13% Cr–4% Ni stainless steel weld by neutron diffraction and the contour method. Materials Science and Engineering: A 2010;527:6205.
[44] Woo W, Feng Z, Wang XL, David SA. Neutron diffraction measurements of residual stresses in friction stir welding: a review. Science and Technology of Welding & Joining 2011;16:23.
[45] Lee SY, Rogge RB, Choo H, Liaw PK. Neutron diffraction measurements of residual stresses around a crack tip developed under variable-amplitude fatigue loadings. Fatigue & Fracture of Engineering Materials & Structures 2010;33:822.
[46] Lee SY, Sun Y, An K, Choo H, Hubbard CR, Liaw PK. Evolution of residual-strain distribution through an overload-induced retardation period during fatigue-crack growth. Journal of Applied Physics 2010;107.
[47] Lee SY, Sun Y, An K, Choo H, Hubbard CR, Liaw PK. Evolution of residual-strain distribution through an overload-induced retardation period during fatigue-crack growth. Journal of Applied Physics 2010;107:023517.
[48] Lee SY, Huang EW, Wu W, Liaw PK, Paradowska AM. Development of crystallographic-orientation-dependent internal strains around a fatigue-crack tip during overloading and underloading. Materials Characterization 2013;79:7.
[49] Owen RA, Preston RV, Withers PJ, Shercliff HR, Webster PJ. Neutron and synchrotron measurements of residual strain in TIG welded aluminium alloy 2024. Materials Science and Engineering a-Structural Materials Properties Microstructure and Processing 2003;346:159.
[50] Poulsen HF, Garbe S, Lorentzen T, Jensen DJ, Poulsen FW, Andersen NH, Frello T, Feidenhansl R, Graafsma H. Applications of high-energy synchrotron radiation for structural studies of polycrystalline materials. Journal of Synchrotron Radiation 1997;4:147.
[51] Reimers W, Broda M, Brusch G, Dantz D, Liss KD, Pyzalla A, Schmackers T, Tschentscher T. Evaluation of residual stresses in the bulk of materials by high energy synchrotron diffraction. Journal of Nondestructive Evaluation 1998;17:129.
[52] Ortner B. Stress measurement in coarse grained material with high-resolution X-ray beams. Thin Solid Films 2013;530:77.
[53] An K, Skorpenske HD, Stoica AD, Ma D, Wang X-L, Cakmak E. First in situ lattice strains measurements under load at VULCAN. Metallurgical and Materials Transactions A 2011;42:95.
[54] Wang X-L, Holden T, Rennich GQ, Stoica A, Liaw PK, Choo H, Hubbard CR. VULCAN—the engineering diffractometer at the SNS. Physica B: Condensed Matter 2006;385:673.
[55] Pussegoda L, Tyson W. Relationship Between Microstructure and Hydrogen Susceptibility of Some Low-Carbon Steels. TMS/AIME 1981:349.
[56] Ellis M, Bartlett R. Effects of Prestrain and Dissolved Hydrogen on the Tensile Properties and the Fracture Behavior of Line-Pipe Steels. Hydrogen Effects on Material Behavior 1989:991.